Article

Mis-splicing of a neuronal microexon promotes CPEB4 aggregation in ASD

https://doi.org/10.1038/s41586-024-08289-w

Received: 9 March 2023

Accepted: 25 October 2024

Published online: 4 December 2024

Open access

Check for updates

Carla Garcia-Cabau[1,10], Anna Bartomeu[1,10], Giulio Tesei[2], Kai Chit Cheung[3], Julia Pose-Utrilla[4,5], Sara Picó[4,5], Andreea Balaceanu[1], Berta Duran-Arqué[1], Marcos Fernández-Alfara[1], Judit Martín[1], Cesare De Pace[6], Lorena Ruiz-Pérez[6,7,8], Jesús García[1], Giuseppe Battaglia[6,7,9], José J. Lucas[4,5], Rubén Hervás[3], Kresten Lindorff-Larsen[2], Raúl Méndez[1,9] ✉ & Xavier Salvatella[1,9] ✉

The inclusion of microexons by alternative splicing occurs frequently in neuronal proteins. The roles of these sequences are largely unknown, and changes in their degree of inclusion are associated with neurodevelopmental disorders[1]. We have previously shown that decreased inclusion of a 24-nucleotide neuron-specific microexon in CPEB4, a RNA-binding protein that regulates translation through cytoplasmic changes in poly(A) tail length, is linked to idiopathic autism spectrum disorder (ASD)[2]. Why this microexon is required and how small changes in its degree of inclusion have a dominant-negative effect on the expression of ASD-linked genes is unclear. Here we show that neuronal CPEB4 forms condensates that dissolve after depolarization, a transition associated with a switch from translational repression to activation. Heterotypic interactions between the microexon and a cluster of histidine residues prevent the irreversible aggregation of CPEB4 by competing with homotypic interactions between histidine clusters. We conclude that the microexon is required in neuronal CPEB4 to preserve the reversible regulation of CPEB4-mediated gene expression in response to neuronal stimulation.

The alternative splicing processes that coordinate the inclusion of neuron-specific microexons are frequently misregulated in individuals with ASD[1,3–5]. We have previously reported that individuals with idiopathic ASD[2] and individuals with schizophrenia[6] show decreased inclusion of a 24-nucleotide microexon (microexon 4 (me4)) in CPEB4. This RNA-binding protein is a member of the cytoplasmic polyadenylation element (CPE) binding (CPEB) family of proteins. These proteins recognize CPEs in 3′ untranslated regions (UTRs) of transcripts and mediate their polyadenlytion and deadenylation, which in turn regulates translation through the assembly of translation–regulation ribonucleoprotein complexes[7]. CPEBs participate in mRNA transport and localization[8,9] and have important roles in cell division, neural development, learning and memory. They can be classified into two subfamilies that differ in the motifs that they recognize in mRNAs, their interactions with other proteins and their regulation. The carboxy-terminal RNA-binding domains of CPEBs are globular, whereas the amino-terminal domains (NTDs) are intrinsically disordered[7,10,11]. Moreover, in cycling cells, the phosphorylation of multiple serine and threonine residues in the NTDs of CPEB2–CPEB4 by ERK2 and CDK1 activates these proteins by dissolving the translation–repression condensates that they form[7,11].

Targets of neuronal CPEB4 (nCPEB4) include transcripts encoded by numerous ASD genes[2]. Meanwhile, a mouse model that harbours an isoform imbalance that favours the expression of a nCPEB4 isoform lacking me4 (nCPEB4Δ4) recapitulates the defects in mRNA polyadenylation and protein expression observed in individuals with ASD and displays ASD-like neuroanatomical, electrophysiological and behavioural phenotypes[2]. nCPEB4Δ4 is dominant-negative in this cell type[2] but not in non-neuronal tissues, where it is active. Despite the association of CPEB4 mis-splicing with disease, the mechanism by which the decreased inclusion of me4 leads to the misregulation of gene expression in ASD is unclear[12]. Here we studied the molecular basis of nCPEB4 activation during depolarization and how the absence of me4 from the intrinsically disordered NTD (Extended Data Fig. 1a) affects the properties of nCPEB4 translation–repression condensates. In contrast to the results obtained in cycling cells, we show that the condensates dissolve after neuron depolarization owing to changes in the intracellular pH that alter the balance of interactions that stabilize the condensates. In addition, the decreased inclusion of me4 in neuron-like cells increases the propensity of the translation–repression condensates to convert into aggregates that do not dissolve after depolarization and that accumulate in the brain in a transgenic mouse model. me4 enables the reversible condensation of nCPEB4 by interacting with a cluster of histidine residues, thereby competing with interactions between clusters that drive aggregation. In summary, we show how

[1]Institute for Research in Biomedicine (IRB Barcelona), The Barcelona Institute of Science and Technology, Barcelona, Spain. [2]Structural Biology and NMR Laboratory, Linderstrøm-Lang Centre for Protein Science, Department of Biology, University of Copenhagen, Copenhagen, Denmark. [3]School of Biomedical Sciences, Li Ka Shing Faculty of Medicine, The University of Hong Kong, Pokfulam, Hong Kong SAR. [4]Center for Molecular Biology Severo Ochoa (CBM Severo Ochoa), CSIC/UAM, Madrid, Spain. [5]Networking Research Center on Neurodegenerative Diseases (CIBER-NED), Instituto de Salud Carlos III, Madrid, Spain. [6]Department of Chemistry and Institute for Physics of Living Systems, University College London, London, UK. [7]Institute for Bioengineering of Catalonia (IBEC), The Barcelona Institute of Science and Technology, Barcelona, Spain. [8]Department of Applied Physics, University of Barcelona, Barcelona, Spain. [9]Catalan Institution for Research and Advanced Studies (ICREA), Barcelona, Spain. [10]These authors contributed equally: Carla Garcia-Cabau, Anna Bartomeu. ✉e-mail: raul.mendez@irbbarcelona.org; xavier.salvatella@irbbarcelona.org

me4 ensures the proper regulation of nCPEB4 and suggest why a reduction in its degree of inclusion in ASD results in a dominant-negative decrease in CPEB4 activity.

Regulation of nCPEB4 condensation

CPEB4 is expressed in most tissues but more abundantly in the nervous system[13] (Extended Data Fig. 1b). The inclusion of me4 in nCPEB4 is limited to neuronal tissues (Extended Data Fig. 1c), where SRRM4, a neuron-specific alternative splicing regulator required for microexon inclusion programs[3,5], is expressed (Extended Data Fig. 1d). We generated a mEGFP–CPEB4 knock-in mouse model (Fig. 1a) from which we obtained primary striatal neurons (Fig. 1b). Imaging of endogenous CPEB4 in neurons revealed a granular distribution of CPEB4 in the cytoplasm (Fig. 1c,d) reminiscent of the condensates formed by overexpressed CPEB4 in non-neuronal cells[7,11]. We used mouse neural crest-derived neuroblastoma Neuro2a (N2a) cells to further study the properties of these foci. These cells recapitulated the neuron-specific and SRRM4-dependent regulation of CPEB4 alternative splicing (Extended Data Fig. 1e–g and Methods), and their neuronal differentiation was induced by retinoic acid[14]. Overexpression of full-length (FL) GFP-tagged nCPEB4 in N2a cells led to the formation of condensates that recovered well in fluorescence recovery after photobleaching (FRAP) experiments and were equivalent to the foci formed by endogenous CPEB4 in neurons. In addition, as in *Xenopus laevis*, the NTD recapitulated the properties of the FL protein[11] (Fig. 1e,f and Extended Data Fig. 1h).

Because neuron stimulation can increase mRNA polyadenylation[15], we investigated whether depolarization alters the properties of the nCPEB4 foci. Depolarization of ex vivo neurons using KCl (Fig. 1g,h and Supplementary Video 1) or NMDA (Extended Data Fig. 1i–k) led to the dissolution of the foci. N2a cells were depolarized by KCl, which caused the dissolution of condensates formed by either nCPEB4(FL) or nCPEB4(NTD) (Fig. 1i,j), but were not depolarized by NMDA (Extended Data Fig. 1k,l). As the NTD of nCPEB4 recapitulated the condensation properties of the FL protein in N2a cells, we studied the condensation of this domain in vitro. The NTD condensed after heating (Extended Data Fig. 1m), and the resulting condensates fused and efficiently recovered in FRAP experiments[11] (Extended Data Fig. 1n,o). Altogether, we conclude that nCPEB4 localizes in cytoplasmic condensates that dissolve after neuron depolarization, reminiscent of the dissolution of the translation–repression CPEB4 condensates that occurs in mitotic cells[7,11] after CPEB4 phosphorylation.

We used mass spectrometry to investigate whether post-translational modifications (PTMs) cause the dissolution of nCPEB4 condensates after depolarization of N2a cells. We detected 11 phosphorylation events of the NTD, including 5 previously identified in non-neuronal cells after mitotic entry[7,11], and 9 methylation events in RNA recognition motifs (RRMs). The general degree of modification was, however, low and invariant after depolarization (Extended Data Fig. 2a,b). Notably, non-phosphorylatable variants of nCPEB4 continued to dissolve after depolarization (Extended Data Fig. 2c–e and Methods). Finally, as depolarization involves calcium mobilization, we treated differentiated N2a cells with the ionophore ionomycin, but did not observe dissolution of the nCPEB4 condensates (Extended Data Fig. 2f,g). In summary, although PTMs such as phosphorylation can lead to the dissolution of CPEB4 condensates in cycling cells[7,11], our results indicate that the dissolution of the condensates formed by nCPEB4 in N2a cells, and consequently the switch from translational repression to activation, is not regulated by phosphorylation events of this protein or by calcium mobilization.

It has been proposed that neuronal depolarization causes a rapid decrease in intracellular pH followed by a slower, longer-lasting increase[16,17]. In both ex vivo neurons and in N2a cells, nCPEB4 condensates responded to depolarization by growing in size before dissolving, with dynamics similar to those proposed for pH changes (Fig. 2a,b and Extended Data Figs. 1i,j and 2h). To investigate how depolarization affects the intracellular pH of N2a cells, we used the pH-sensitive dye SNARF-5F. In the majority of cells, depolarization caused a decrease in pH of approximately 0.08 units, lasting for approximately 10 min, followed by a slow increase in pH of up to 0.3 units (Fig. 2c and Extended Data Fig. 2i). We next used NMR to determine the pK_a values of the histidine side chains of nCPEB4(NTD), which is enriched in this residue type (Extended Data Fig. 2j). The pK_a values

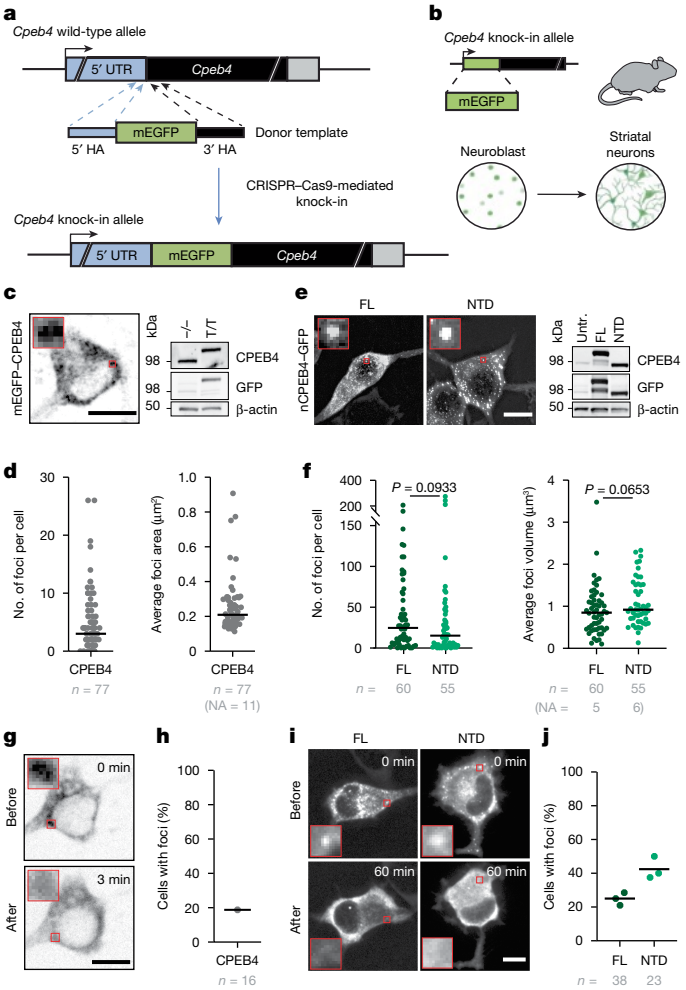

Fig. 1 | CPEB4 condenses in neurons. a, CRISPR–Cas9-mediated mEGFP knock-in strategy in mice. **b**, Generation of ex vivo differentiated striatal neurons from mEGFP–CPEB4 knock-in mice. **c**,**d**, Fluorescence microscopy image of live ex vivo primary striatal neurons (left) and western blot (right) analysing mEGFP–CPEB4 expression (**c**) and the number and size of foci (**d**) (median). −/−, untagged littermates; NA, not applicable; T/T, mEGFP–CPEB4 mice. *n*, cells. **e**,**f**, Fluorescence microscopy image of fixed differentiated N2a cells overexpressing nCPEB4 (left) and western blot (right) analysing FL and NTD expression (**e**) and the number and size of foci (**f**) (median, two-tailed Mann–Whitney test). Untr., untransfected cells. *n*, cells from 3 independent experiments. **g**,**h**, Fluorescence microscopy images of live ex vivo primary striatal neurons before and after stimulation (**g**) and percentage of cells (mean) with foci after stimulation (3 min) (**h**). *n*, cells. **i**,**j**, Fluorescence microscopy images of live differentiated N2a cells overexpressing nCPEB4–GFP before and after stimulation (**i**) and percentage of cells (mean) with foci after stimulation (60 min) (**j**). *n*, cells from 3 independent experiments. For **h** and **j**, only cells with cytoplasmic foci before stimulation were analysed. For gel source data, see Supplementary Fig. 1. Scale bars, 10 µm (**c**,**e**,**g**,**i**). Illustration in **b** created using BioRender (credit: R.M., https://biorender.com/q00q129; 2024).

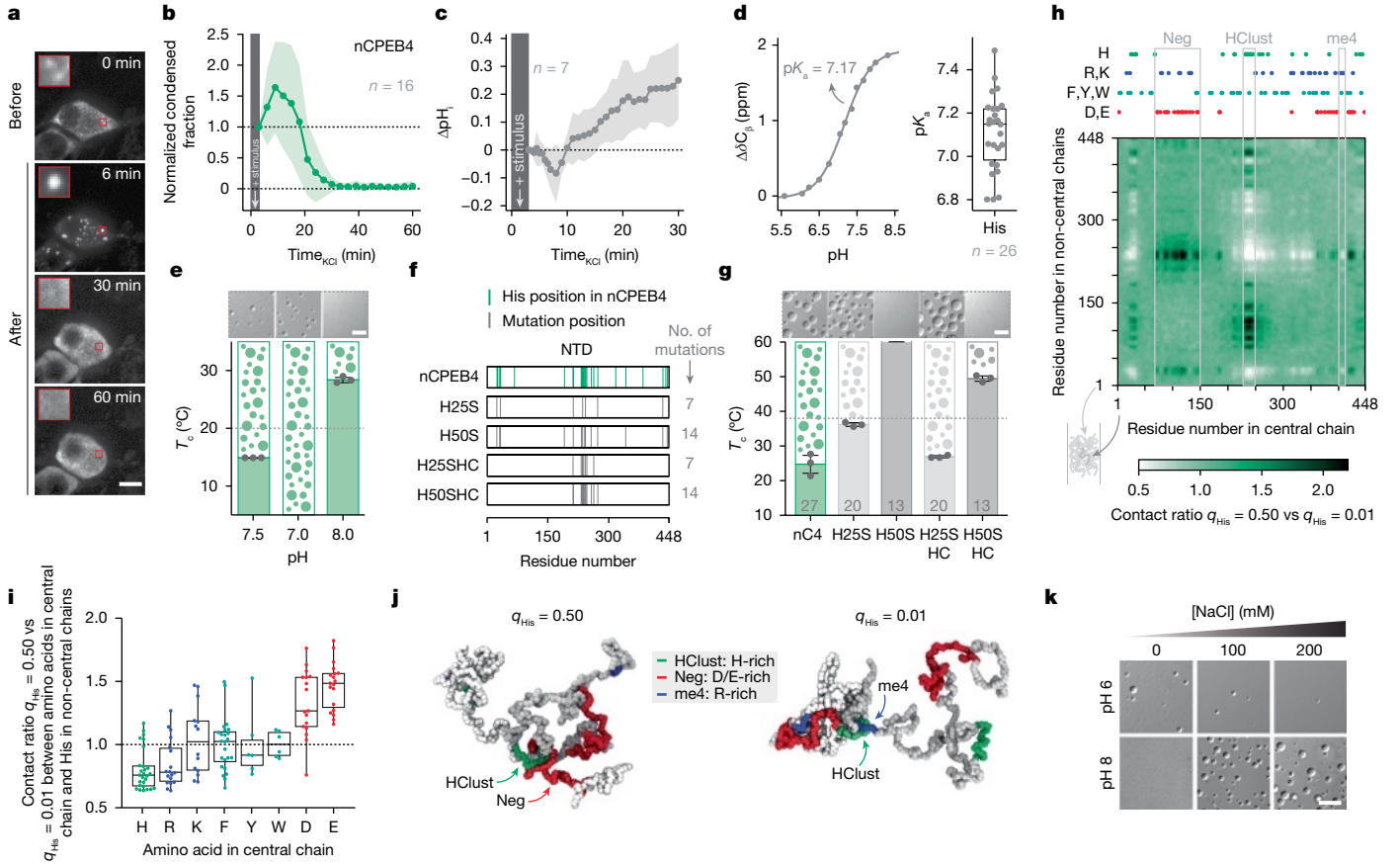

Fig. 2 | nCPEB4 condensation is regulated by pH. a,**b**, Fluorescence microscopy images of live differentiated N2a cells overexpressing FL nCPEB4–GFP before and after stimulation (**a**) and the fraction of cellular area occupied by condensates after stimulation, normalized to the value measured at the end of stimulation (**b**). Representation of the most common behaviour (53.3% of cells, mean ± s.d.). *n*, cells out of 30 cells. **c**, Changes in intracellular pH of N2a cells after stimulation. Representation of the most common behaviour (53.8% of cells, mean ± s.d.). *n*, cells out of 13 cells from 3 independent experiments. **d**, Chemical shift of a specific nCPEB4(NTD) histidine C_β signal as a function of pH and pK_a values of all histidine side-chain resonances. Box plots: line, median; box, quartiles; whiskers, 1.5× the interquartile range. *n*, resonances. **e**, Differential interference contrast (DIC) microscopy images at 20 °C (top) and cloud points (bottom; mean ± s.d.) of nCPEB4(NTD) as a function of pH (10 µM protein, 100 mM NaCl). *n* = 3 independent measurements. **f**, nCPEB4(NTD) mutants. **g**, DIC microscopy images at 38 °C (top) and cloud points (bottom; mean ± s.d.) of nCPEB4(NTD) and mutants (30 µM protein, 100 mM NaCl, pH 8). The number of histidine residues is indicated at the base of each bar. nC4, nCPEB4. *n* = 3 independent measurements. **h**, Map of intermolecular contact ratios, after histidine protonation, between a chain in the middle of the condensate and the surrounding chains (mean). Neg, region rich in negatively charged amino acids; q_{His}, charge of histidine residues. *n* = 3 independent simulation replicas. **i**, Contact ratio between different residue types on a chain in the middle of the condensate and the histidine residues on the surrounding chains (mean). Box plots: line, median; box, quartiles; whiskers, rest of the distribution. *n* = 3 independent simulation replicas. **j**, Simulation snapshots of two interacting nCPEB4(NTD) chains in a condensate. **k**, DIC microscopy images of nCPEB4(NTD) as a function of pH and NaCl concentration at 25 °C (5 µM protein for pH 6; 30 µM protein for pH 8). *n* = 3 fields of view. For **b**, only cells with cytoplasmic foci before stimulation were analysed. Scale bars, 10 µm (**a**,**e**,**g**,**k**).

ranged from 6.8 to 7.5 depending on the resonance monitored, with a mean value of 7.1 (Fig. 2d and Extended Data Fig. 2k). Next, we studied whether pH influences the condensation of nCPEB4(NTD) in vitro. A comparison of the cloud point (T_c) values of a nCPEB4(NTD) solution at pH 7.5 with that of the same sample at lower (7.0) and higher (8.0) pH values led to a decrease and increase, respectively (Fig. 2e). Finally, we studied constructs in which 25% or 50% of histidine amino acid residues were substituted by serine, a residue with similar hydrogen-bonding properties but lacking an aromatic ring, either throughout the sequence (H25S and H50S, respectively) or in the cluster of histidine residues (HClust) centered on position 240 (H25SHC and H50SHC, respectively) (Fig. 2f). These substitutions lowered the condensation propensities of the constructs (Fig. 2g). This result indicates that, as observed for other intrinsically disordered proteins rich in aromatic residues[18–21], the aromatic character of histidine residues governs the condensation propensity of nCPEB4(NTD), which is probably due to their ability to interact with aromatic and positively charged residues.

We interrogated the CALVADOS residue-level model[22,23] (Extended Data Fig. 3a,b) to determine the effect of increasing the degree of protonation (q_{His}) on the intermolecular contacts within simulated condensates. The ratio between the contacts from simulations corresponding to q_{His} = 0.50 compared with q_{His} = 0.01 (Fig. 2h) revealed a rearrangement of the network of interactions that favoured contacts between histidines and residues located in regions rich in aspartate and glutamate (residues 72–147 and 424–448) when the histidine residues are protonated. Conversely, contacts between histidines and arginine residues in me4 (residues 403–410) were favoured when they are not (Fig. 2i,j and Extended Data Fig. 3c). To confirm that protonation modulates the interactions that drive condensation, we assessed the effect of ionic strength on the stability of the condensates in vitro (Fig. 2k and Extended Data Fig. 3d). At pH 8, an increase in ionic strength promoted condensation, probably by shielding repulsive electrostatic interactions and enhancing hydrophobic interactions[24]. At pH 6, by contrast, we obtained the opposite result, which is in agreement with the notion that attractive electrostatic interactions stabilize the condensates.

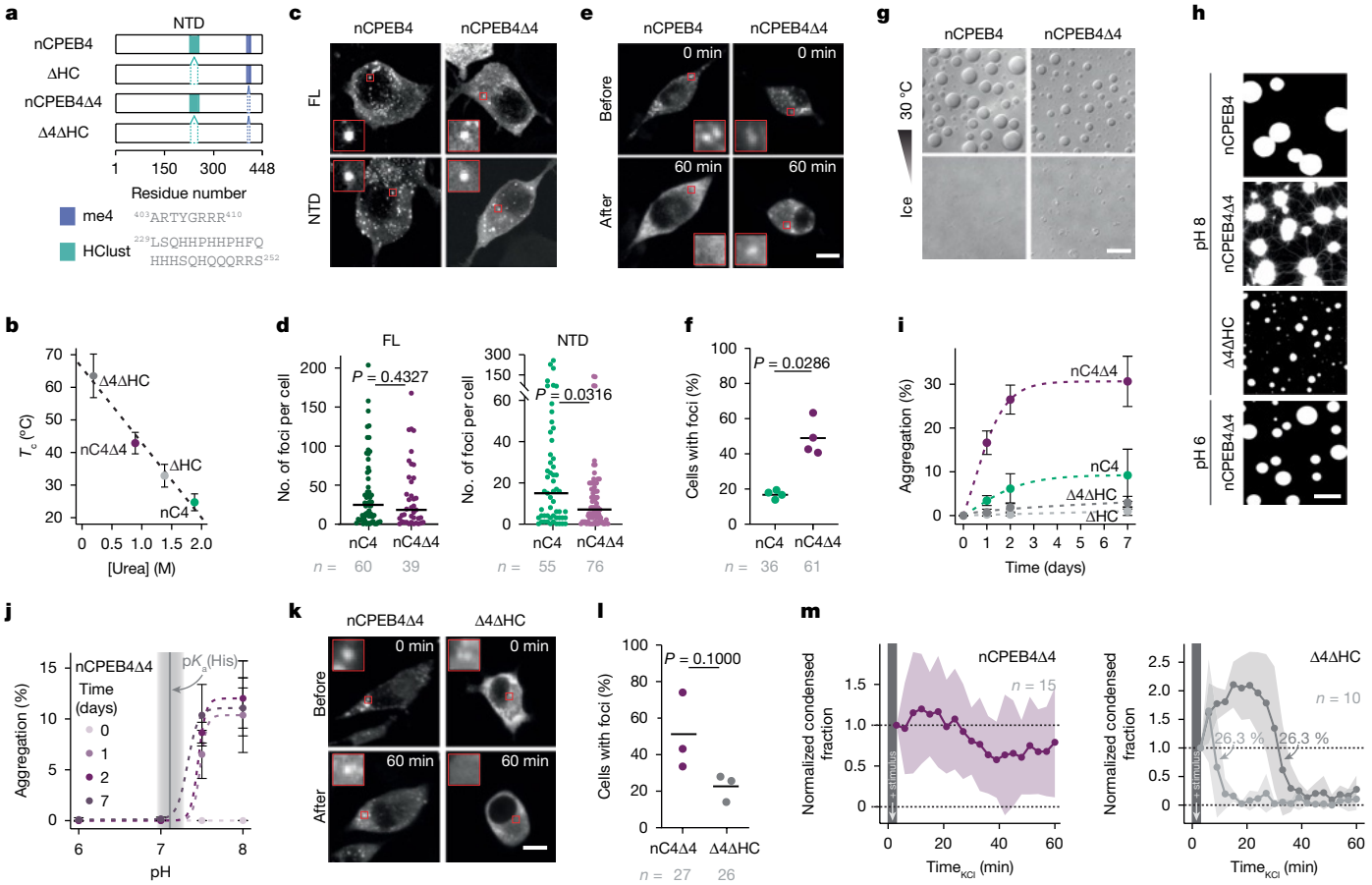

Fig. 3 | me4 prevents CPEB4 aggregation. a, nCPEB4(NTD) deletion variants. **b**, Cloud points (mean ± s.d., $n = 3$ independent measurements; 30 µM protein, 100 mM NaCl) and urea concentration required for multimer dissolution (100 µM protein, 5 °C; Extended Data Fig. 4a). **c**,**d**, Fluorescence microscopy images of fixed differentiated N2a cells overexpressing nCPEB4–GFP or nCPEB4Δ4–GFP (**c**) and number of foci (median, two-tailed Mann–Whitney test) (**d**). *n*, cells from 3 independent experiments. **e**,**f**, Fluorescence microscopy images of live differentiated N2a cells overexpressing nCPEB4–GFP or nCPEB4Δ4–GFP before and after stimulation (**e**) and percentage of cells (mean, two-tailed Mann–Whitney test) with foci after stimulation (60 min) (**f**). *n*, total cells analysed by blind analysis from a pool of 7 experiments. **g**, DIC microscopy images of nCPEB4(NTD) and nCPEB4Δ4(NTD) at 30 °C and on ice (30 µM protein, 150 mM NaCl). $n = 3$ fields of view. **h**, Fluorescence microscopy images (with enhanced brightness) of nCPEB4(NTD) and mutants after 1 day of incubation (30 µM protein, 200 mM NaCl, 37 °C). $n = 9$ fields of view from 3 independent experiments. **i**,**j**, Aggregation quantification (mean ± s.d.) of nCPEB4(NTD) and variants (**i**) and of nCPEB4Δ4(NTD) as a function of pH (**j**) (30 µM protein, 200 mM NaCl, 37 °C). $n = 9$ fields of view from 3 independent experiments. Vertical line and shading indicate mean ± s.d. of the His pK_a values (Fig. 2d). **k**,**l**, Fluorescence microscopy images of live differentiated N2a cells overexpressing nCPEB4Δ4–GFP or Δ4ΔHC–GFP before and after stimulation (**k**) and percentage of cells (mean, two-tailed Mann–Whitney test) with foci after stimulation (60 min) (**l**). *n*, cells from 3 independent experiments. **m**, Fraction of the cellular area occupied by condensates after stimulation, normalized to the value measured at the end of stimulation. Left, representation of the most common behaviour (68.2% of cells, mean ± s.d.) of nCPEB4Δ4. *n*, cells out of 22 cells. Right, representation of the most common behaviours (52.6% of cells, mean ± s.d.) of Δ4ΔHC. *n*, cells out of 19 cells. For **f**, **l** and **m**, only cells showing cytoplasmic foci before stimulation were analysed. nC4, nCPEB4; nC4Δ4, nCPEB4Δ4. Scale bars, 10 µm (**c**,**e**,**g**,**h**,**k**).

me4 prevents CPEB4 aggregation

To better understand which specific residues of nCPEB4(NTD) drive condensation, we used solution NMR spectroscopy. At high pH and at temperatures below the T_c, nCPEB4(NTD) formed multimers with a hydrodynamic diameter of approximately 55 nm and stabilized by interactions similar to those stabilizing the condensates. The NMR spectra of the multimers, interpreted with the help of molecular simulations, revealed that multimerization is driven by interactions between histidine and arginine side chains, including interactions between HClust (residues 229–252) and me4, which is rich in arginine residues (residues 403–410) (Extended Data Fig. 3e–m, Supplementary Fig. 5 and Methods). To investigate the roles of these two regions of sequence in multimerization and condensation, we studied deletion variants of nCPEB4(NTD) that lack HClust (ΔHC), me4 (nCPEB4Δ4) or both regions (Δ4ΔHC) (Fig. 3a). The deletion mutants decreased the multimerization and condensation propensity of nCPEB4 (Fig. 3b, Extended Data Figs. 3i and 4a), which implied that me4 and HClust are engaged in intermolecular interactions. Therefore, the multimers and the condensates formed by nCPEB4Δ4(NTD) have decreased relative stability compared with nCPEB4(NTD) due to the loss of 4 of the 18 arginine residues present in this domain (Extended Data Fig. 4b–d). Finally, we measured the number and size of the condensates formed by nCPEB4 and nCPEB4Δ4 in N2a cells. The former formed more condensates than the latter in the context of the NTD, although the differences were smaller for the FL protein (Fig. 3c,d and Extended Data Fig. 4e). Other ASD-related microexons, for example, those found in the translation regulator eIF4G, regulate the neural proteome by promoting coalescence with neuronal granule components[5]. To address whether me4 has a similar effect, we analysed the interactomes of both nCPEB4 and nCPEB4Δ4 and found that they showed similar interactions with other proteins (Extended Data Fig. 4f,g). In addition, both nCPEB4 and nCPEB4Δ4 showed similar binding to RNA (Extended Data Fig. 4h). These findings suggest that the decreased propensity of nCPEB4Δ4

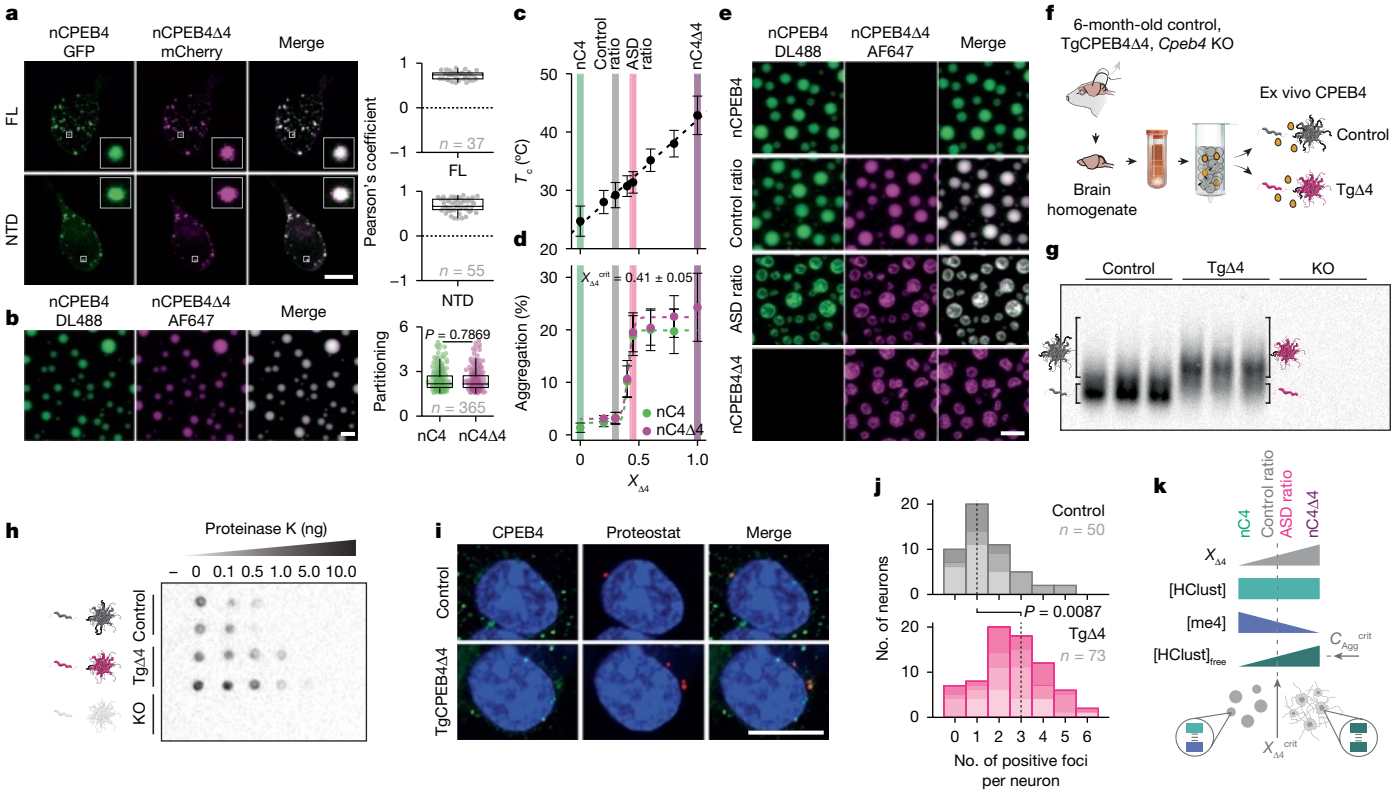

Fig. 4 | Dominant-negative effect of mis-splicing. a, Fluorescence microscopy images of fixed differentiated N2a cells co-transfected with nCPEB4–GFP and nCPEB4Δ4–mCherry (left) and co-localization, as assessed by using Pearson's correlation coefficient (right). Box plots: line, median; box, quartiles; whiskers, 1.5× interquartile range. *n*, cells from 3 independent experiments. **b**, Fluorescence microscopy images of a solution of nCPEB4(NTD) and nCPEB4Δ4(NTD) ($\chi_{\Delta4}$ = 0.5, *n* = 3 fields of view; left) and partitioning in the condensates (*n*, condensates, two-tailed Mann–Whitney test; right) (30 µM protein, 200 mM NaCl, 37 °C). Box plots: line, median; box, quartiles; whiskers, 1.5× interquartile range. **c**, Cloud point of solutions of nCPEB4(NTD) and nCPEB4Δ4(NTD) of different compositions (mean ± s.d.) (20 µM protein, 100 mM NaCl). *n* = 3 independent measurements. **d**,**e**, Aggregation quantification (mean ± s.d.) after 1 day (**d**) and fluorescence microscopy images of nCPEB4, nCPEB4Δ4 and ratios of control and ASD (**e**) (30 µM protein, 200 mM NaCl, 37 °C). *n* = 10 fields of view from 3 independent experiments. **f**, Schematic of analysis of aggregates in mouse brains. Yellow spheres, co-purified entities. **g**, Western blot of ex vivo CPEB4 from brains of 6-month-old control mice, TgCPEB4Δ4 mice and *Cpeb4* knockout mice (KO; negative control) by SDD–AGE, with the positions of monomeric and aggregated CPEB4 indicated. *n* = 2 individual measurements. **h**, Dot blot western of proteinase K resistance of CPEB4 from brains of 6-month-old control mice, TgCPEB4Δ4 mice and *Cpeb4* KO mice. *n* = 2 individual measurements. **i**,**j**, Fluorescence microscopy images of striatal neurons from brain sections of 1.5-month-old control mice and TgCPEB4Δ4 mice immunostained for CPEB4 (green) and co-staining with Proteostat dye (red) for aggregates (**i**) and distribution of the number of double-positive (CPEB4 and Proteostat) foci per neuron (**j**). *n*, neurons from 3 (control) and 4 (TgCPEB4Δ4) mice (colour shades). Dotted line: median. Significance assessed using a generalized linear mixed model. **k**, Effect of $\chi_{\Delta4}$ on the aggregation of mixtures of nCPEB4(NTD). C_{Agg}^{crit}, critical concentration of free HClust necessary for aggregation, defining $\chi_{\Delta4}^{crit}$; $[HClust]_{free}$, amount of HClust not interacting with me4. For gel source data, see Supplementary Fig. 4. nC4, nCPEB4; nC4Δ4, nCPEB4Δ4; TgΔ4, TgCPEB4Δ4. Scale bars, 10 µm (**a**,**b**,**e**,**i**).

to form condensates in N2a cells is intrinsic to its sequence and is not due to differences in interactions with other proteins or with RNA.

As the nCPEB4 condensates stabilized in part by me4 are translation–repressive, our results do not explain how its loss leads to the decrease in nCPEB4 activity observed in ASD models and in individuals with ASD. We therefore assessed how me4 influences dissolution of the condensates after depolarization (Fig. 3e). Condensates formed in N2a cells overexpressing nCPEB4Δ4 dissolved in a lower fraction of cells: although 17% of cells had condensates after depolarization of nCPEB4, this value increased to 49% after me4 deletion (Fig. 3f and Extended Data Fig. 5a). This result implied a decrease in the reversibility of condensation in the absence of me4. This difference was not due to PTMs, which did not change in either variant after depolarization (Extended Data Fig. 5b), or to an intrinsically different response to the effect of pH on condensation propensity (Extended Data Fig. 5c). Next, we studied the effect of me4 on the reversibility of nCPEB4(NTD) condensation in vitro. As expected, decreasing the temperature of a sample of nCPEB4(NTD) condensates led to their dissolution. By contrast, in the absence of me4, dissolution was only partial, an effect that may be due to aggregation (Fig. 3g). We next analysed the fate of the condensates formed by nCPEB4 and nCPEB4Δ4 by fluorescence microscopy after 1 day of incubation in vitro. The condensates formed by nCPEB4Δ4 transitioned into aggregates in the absence and in the presence of RNA, which showed no fluorescence recovery in FRAP experiments (Fig. 3h,i, Extended Data Fig. 5d–g and Methods).

An alignment of the sequences of nCPEB4 and Orb2b (its *Drosophila melanogaster* orthologue) revealed that HClust shares features with the endogenous Orb2 amyloid core characterized by cryogenic electron microscopy[25] (Supplementary Data). We therefore proposed that HClust drives the aggregation of nCPEB4. Indeed, we observed that its deletion from nCPEB4Δ4(NTD) (Δ4ΔHC) prevented aggregation (Fig. 3h,i and Extended Data Fig. 5d). To strengthen this conclusion, we measured the effect of pH on aggregation. The condensates remained dynamic at pH values lower than the pK_a of histidine side chains (Fig. 2d), and aggregation occurred at pH values at which the histidine residues are uncharged. This effect is presumably because the lack of repulsive interactions between positively charged histidine side chains facilitates homotypic interactions between HClust regions in different nCPEB4 molecules[26] (Fig. 3j). For clarity, in this work, we define homotypic and heterotypic interactions as those taking place between

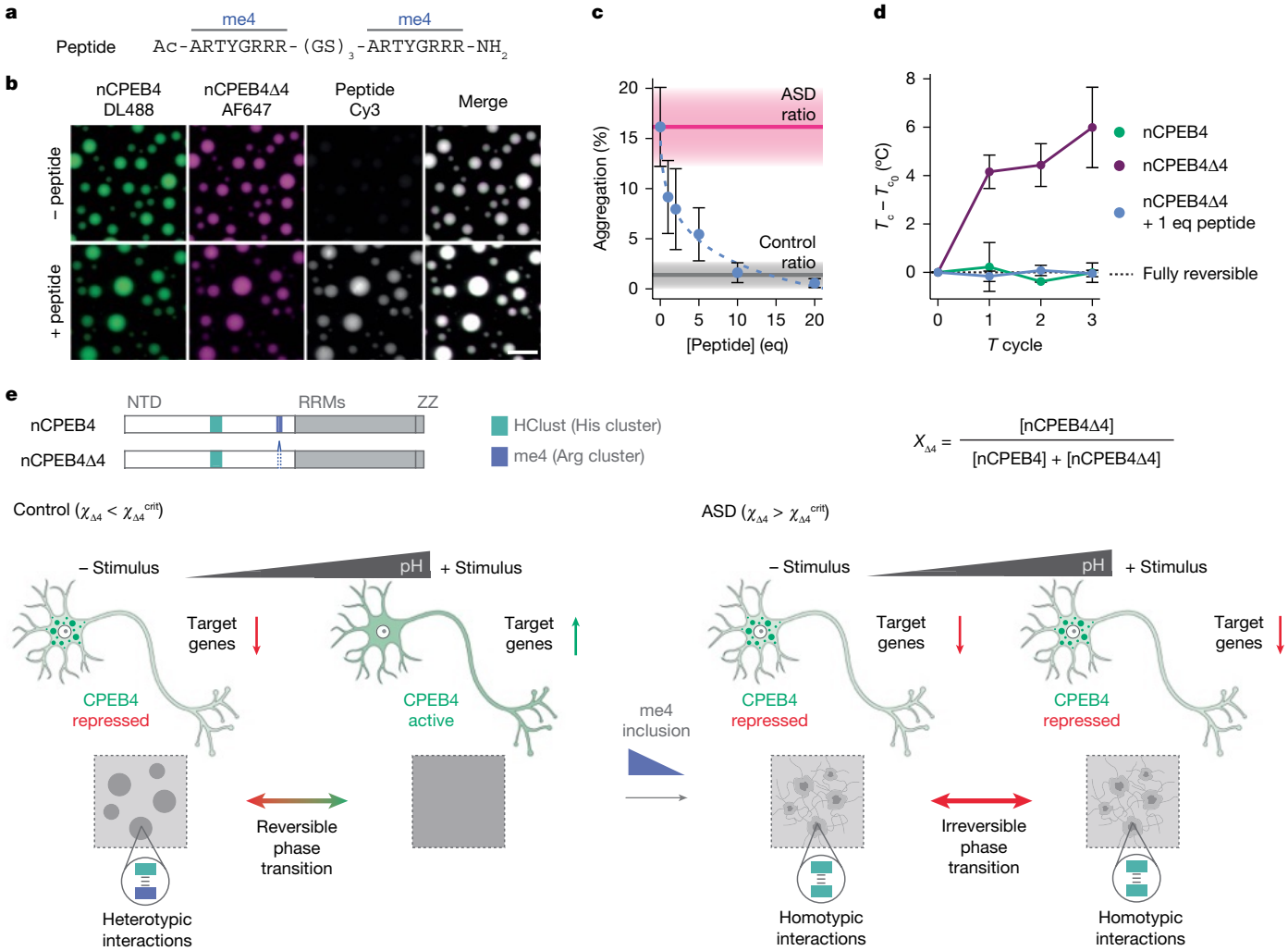

Fig. 5 | A peptide restores the reversibility of condensation. a, Peptide sequence. **b**, Fluorescence microscopy images of an ASD ratio sample in the absence (−peptide) and presence (+peptide) of 1 molar equivalent (eq) of peptide (30 µM protein, 100 mM NaCl, 37 °C). $n = 3$ fields of view. Scale bar, 10 µm. **c**, Aggregation quantification of nCPEB4Δ4–AF647 in an ASD ratio sample at increasing molar equivalents of peptide after 1 day (mean ± s.d.) (30 µM protein, 100 mM NaCl, 37 °C). $n = 9$ fields of view from 3 independent experiments. **d**, Temperature reversibility experiment monitored by apparent absorbance measurements. Change of the cloud point (mean ± s.d.) at each temperature cycle, relative to that measured before the first cycle ($T_c - T_{c0}$) (20 µM protein, 100 mM NaCl). $n = 3$ independent measurements. Dotted line: fully reversible process. **e**, Schematic illustration of how low inclusion of me4 in nCPEB4 can lead to the onset of ASD. Illustration in **e** created using BioRender (credit: R.M., https://biorender.com/j24j695; 2022).

equivalent or different motifs, respectively, independently of whether they are found in the same or a different protein molecule[27]. Together, these results indicate that HClust is responsible for nCPEB4Δ4(NTD) aggregation in vitro and that me4 inhibits it in nCPEB4(NTD). To test this hypothesis in N2a cells, we assessed the effect of deleting HClust from nCPEB4Δ4. We observed a decrease in the fraction of cells with condensates remaining after depolarization from 50% to 22% (Fig. 3k,l), which caused this protein variant to behave similarly to nCPEB4 (Fig. 3m and Extended Data Fig. 5h). Taken together, these observations suggest that me4 kinetically stabilizes nCPEB4 translation–repression condensates against HClust-driven aggregation, which facilitates their dissolution after depolarization.

Dominant-negative effect of mis-splicing

nCPEB4 and nCPEB4Δ4 are co-expressed in neurons, and small increases in the mole fraction of nCPEB4Δ4 can have a dominant-negative effect on the translation of the mRNAs regulated by nCPEB4 in ASD[2]. To provide a molecular mechanism for this phenomenon, we first studied whether the two isoforms coexist in the same condensates. Co-expression of nCPEB4 and nCPEB4Δ4 in N2a cells, and in vitro experiments carried out with purified variants, showed that they co-localize and have similar dynamics and partition coefficients (Fig. 4a,b and Extended Data Fig. 6a,b). Next, to study the properties of condensates containing both isoforms in vitro, we prepared samples at mole fractions ($\chi_{\Delta4}$) ranging between 0—corresponding to pure nCPEB4(NTD)—and 1—corresponding to pure nCPEB4Δ4(NTD). The T_c values depended linearly on $\chi_{\Delta4}$, which resulted in similar T_c values for the average mole fractions, in terms of mRNA levels, of unaffected individuals[2] (control ratio, $\chi_{\Delta4} = 0.30$) and individuals with ASD[2] (ASD ratio, $\chi_{\Delta4} = 0.45$) (Fig. 4c). We next used fluorescence microscopy to measure the degree of aggregation of the same mixtures after 1 day of incubation. We obtained values between those of pure nCPEB4(NTD) and pure nCPEB4Δ4(NTD). However, contrary to the linear dependence of T_c on $\chi_{\Delta4}$, the dependence of aggregation on $\chi_{\Delta4}$ was sigmoidal (Fig. 4d and Extended Data Fig. 6c), and the threshold value of $\chi_{\Delta4}$ triggering aggregation was between that corresponding to the control and ASD ratios (Fig. 4e). Although these values represent the averages of relatively broad distributions of mRNA levels[2], the sigmoidal dependence provides a plausible rationale of why small changes in $\chi_{\Delta4}$ caused by mis-splicing can lead to abrupt

changes in activity of this protein and, potentially, to the onset of ASD. Notably, changes in $\chi_{\Delta4}$ did not seem to alter the ability of the mixtures to respond to pH changes, and incubation of such mixtures at pH 6 did not result in aggregation. This result supports the notion that homotypic interactions between HClust regions—weakened by histidine side-chain protonation—are responsible for the loss of the dynamic character of CPEB4 condensates (Extended Data Fig. 6d,e).

Finally, we studied the in vivo conformation of CPEB4 extracted from the brains of 6-month-old control mice and TgCPEB4Δ4 mice, a mouse model of ASD[2] (Fig. 4f and Extended Data Fig. 6f). An analysis using semi-denaturing detergent–agarose gel electrophoresis (SDD–AGE) revealed an increase in SDS-resistant CPEB4 aggregates in the brains of TgCPEB4Δ4 mice compared with brains from age-matched control mice (Fig. 4g). To quantify this effect, we separated the different conformational states of extracted CPEB4 through gel filtration. The results confirmed that CPEB4 forms stable, high-molecular-mass aggregates resistant to proteinase K (Fig. 4h) in the brains of TgCPEB4Δ4 mice, whereas CPEB4 remained mostly soluble in the brains of control mice (Extended Data Fig. 6g). Incubation of trace amounts of SDS-resistant CPEB4 aggregates isolated from TgCPEB4Δ4 mouse brains with soluble CPEB4 from control mouse brains seeded its aggregation into SDS-resistant aggregates in a time-dependent manner (Extended Data Fig. 6h). This result suggests that small changes in the degree of inclusion of me4 can generate a dominant-negative effect on the expression of ASD-linked genes in this neurodevelopmental disorder. We also studied the presence of CPEB4 aggregates in striatal neurons of control mouse and TgCPEB4Δ4 mouse brain slices by using the dye Proteostat, which is specific for protein aggregates. The number of CPEB4 condensates showing signs of aggregation was higher in TgCPEB4Δ4 mice than in control mice (Fig. 4i,j). Collectively, these in vivo findings indicate that an imbalance in CPEB4 isoforms drives the aggregation of this protein in the brain of an ASD-relevant mouse model.

Our results suggest that the arginine residues of me4 inhibit aggregation by kinetically stabilizing nCPEB4 condensates relative to aggregates by shifting the balance between homotypic and heterotypic interactions[26]. The boundary between the condensed and aggregated regimens corresponded to the value of $\chi_{\Delta4}$ associated with the minimal concentration of free HClust ($C_{\mathrm{Agg}}{}^{\mathrm{crit}}$), not interacting with me4, that must be reached for aggregation in our experimental time scale (Fig. 4k). In this scenario, it would be possible to reduce the rate of aggregation by decreasing the concentration of free HClust in the condensates. To this end, we designed a synthetic peptide that contained two repetitions of the sequence of me4 (Fig. 5a) and studied its effect on the condensates formed by a sample with the composition associated with ASD. The peptide partitioned into the condensates (Fig. 5b and Extended Data Fig. 7a), increased their thermodynamic stability (Extended Data Fig. 7b) and decreased aggregation in a concentration-dependent manner (Fig. 5c and Extended Data Fig. 7c). To confirm that the lack of reversibility of nCPEB4Δ4(NTD) condensation is associated with aggregation, we carried out repeated temperature cycles consisting of heating, cooling and centrifugation steps (Extended Data Fig. 7d). For nCPEB4(NTD), the T_c measured for each cycle was constant ($T_{ci} \approx T_{c0}$), which indicated that condensation was fully reversible. By contrast, for nCPEB4Δ4(NTD), it progressively increased ($T_{ci+1} > T_{ci}$), which indicated that the dissolution of the condensates was incomplete as a result of aggregation. The addition of 1 molar equivalent of the peptide to the nCPEB4Δ4(NTD) sample led to full recovery of the reversibility of condensation (Fig. 5d and Extended Data Fig. 7e,f), a result in agreement with our hypothesis.

Discussion

me4, rich in arginine residues, increases the kinetic stability of condensed CPEB4 by interacting with a cluster of histidine residues in the centre of its NTD (HClust, residues 229–252). This heterotypic interaction is necessary for the expression of ASD-linked neurodevelopmental genes because it preserves the reversibility of CPEB4 condensation, the process that regulates their translation. Indeed, in the absence of me4, homotypic interactions between histidine clusters led to the irreversible aggregation of CPEB4. This finding illustrates how a failure of heterotypic buffering, a generic mechanism to preserve the dynamic character of biomolecular condensates in cells[26,28], can lead to protein aggregation and disease[29–33] (Fig. 5e).

nCPEB4 and nCPEB4Δ4 coexist in neurons, and the changes in the polyadenylation of ASD genes associated with this disorder are caused by a subtle decrease in the degree of inclusion of me4, which generates a dominant-negative effect[2]. We showed that the propensity of mixtures of nCPEB4 and nCPEB4Δ4 to aggregate depends on the concentration of histidine clusters available for homotypic interactions. Given that me4 can also engage in interactions with such clusters, thereby competing with homotypic interactions, this concentration decreases with the degree of inclusion of me4. However, the dependence is sigmoidal, thereby indicating that a degree of inclusion of approximately 60% is necessary and sufficient to preserve the liquid character of the condensates and the reversibility of condensation.

We propose that low inclusion of me4 leads to the onset of ASD because it promotes the aggregation of CPEB4, which in turn leads to low CPEB4 activity after neuron depolarization and, as a consequence, low expression of ASD genes[2]. Notably, this mechanism provides a rationale for the dominant-negative effect because a degree of inclusion of me4 below the minimum can lead to the cooperative and irreversible aggregation of both CPEB4 isoforms and, potentially, of other CPEB proteins found in the same condensates. In addition, it suggests that neurons, unlike non-neuronal cells, require a minimal inclusion of me4 in CPEB4 to preserve the liquid character of the translation–repression condensates because they express CPEB4 at particularly high levels. Moreover, the frequency of neuron stimulation is such that nCPEB4 can remain condensed for extended periods of time and nCPEB4 can undergo multiple cycles of condensation and dissolution.

In our previous study, the average ratio of isoforms observed in individuals diagnosed with ASD ($\chi_{\Delta4} = 0.45$) was reproduced in mice by overexpressing nCPEB4Δ4 (ref. 2). At the age at which these mice were analysed, they recapitulated that specific ratio without a net increase in total protein levels, but whether the ratio changes during embryonic neurodevelopment has not yet been analysed. Therefore, it will be interesting in future studies to examine CPEB4 splicing during embryonic neurodevelopment and to generate alternative mouse models that recapitulate ASD events, including the dynamics of splicing ratios, during embryonic neurodevelopment.

Given that the nominal pK_a of the histidine side chain is close to physiological pH, small fluctuations in pH can alter the condensation propensity of proteins enriched in this residue. This property can be used to design pH-sensitive polymers for applications in bioengineering[34,35] and explains how changes in pH alter the phase separation propensity of fillagrin in skin barrier formation[36]. Similarly, stress conditions lead to pH fluctuations that trigger a phase transition in a yeast prion protein through protonation of glutamate residues[37]. In nCPEB4, the changes in condensation propensity and activity that occur after depolarization are caused by local changes in intracellular pH. This mechanism contrasts with how CPEB4 activity is regulated during the cell cycle in non-neuronal cells, in which condensate dissolution is caused by phosphorylation by cell-cycle-specific kinases such as CDK1 (ref. 11).

Notably, CPEB2 and CPEB3 are also enriched in histidine residues (Extended Data Fig. 7g,h) and contain the same neuron-specific microexon, which suggests that our conclusions regarding CPEB4 may apply to other members of this family of translational regulators[38–40]. Moreover, the regulation of the activity of CPEBs may be part of a larger regulatory program controlled by the splicing factor SRRM4, which can affect other proteins bearing microexons dysregulated in ASD such as

eIF4G[5]. The effects of mis-splicing are likely to be microexon-specific and protein-specific and can include changes in phase behaviour, as well as in the interaction with co-factors[5]. Ultimately, the altered translation program in ASD is due to the combined effects of all changes in neuron microexon inclusion that occur in this disorder.

Our work provides an example of how alternative splicing provides a means to tissue-specifically control the material properties of biomolecular assemblies to ensure that key biological activities are properly regulated in different contexts[41–43]. In addition, it reveals how mis-splicing can alter the material properties of such assemblies, thereby leading to disease, and provides proof of concept of how this process can be prevented or reversed. More specifically, our understanding of how reduced inclusion of me4 in CPEB4 generates a dominant-negative effect, and our observation that the normal activity of me4 can be restored in *trans*, opens up an opportunity to treat ASD on the basis of regulation of the dynamics of biomolecular assemblies by drug-like small molecules and peptides[44].

Online content

Any methods, additional references, Nature Portfolio reporting summaries, source data, extended data, supplementary information, acknowledgements, peer review information; details of author contributions and competing interests; and statements of data and code availability are available at https://doi.org/10.1038/s41586-024-08289-w.

1. Gonatopoulos-Pournatzis, T. & Blencowe, B. J. Microexons: at the nexus of nervous system development, behaviour and autism spectrum disorder. *Curr. Opin. Genet. Dev.* **65**, 22–33 (2020).
2. Parras, A. et al. Autism-like phenotype and risk gene mRNA deadenylation by CPEB4 mis-splicing. *Nature* **560**, 441–446 (2018).
3. Irimia, M. et al. A highly conserved program of neuronal microexons is misregulated in autistic brains. *Cell* **159**, 1511–1523 (2014).
4. Ule, J. & Blencowe, B. J. Alternative splicing regulatory networks: functions, mechanisms, and evolution. *Mol. Cell* **76**, 329–345 (2019).
5. Gonatopoulos-Pournatzis, T. et al. Autism-misregulated eIF4G microexons control synaptic translation and higher order cognitive functions. *Mol. Cell* **77**, 1176–1192.e16 (2020).
6. Ollà, I. et al. Pathogenic mis-splicing of CPEB4 in schizophrenia. *Biol. Psychiatry* **94**, 341–351 (2023).
7. Duran-Arqué, B. et al. Comparative analyses of vertebrate CPEB proteins define two subfamilies with coordinated yet distinct functions in post-transcriptional gene regulation. *Genome Biol.* **23**, 192 (2022).
8. Ivshina, M., Lasko, P. & Richter, J. D. Cytoplasmic polyadenylation element binding proteins in development, health, and disease. *Annu. Rev. Cell Dev. Biol.* **30**, 393–415 (2014).
9. Weill, L., Belloc, E., Bava, F.-A. & Méndez, R. Translational control by changes in poly(A) tail length: recycling mRNAs. *Nat. Struct. Mol. Biol.* **19**, 577–585 (2012).
10. Afroz, T. et al. A fly trap mechanism provides sequence-specific RNA recognition by CPEB proteins. *Genes Dev.* **28**, 1498–1514 (2014).
11. Guillén-Boixet, J., Buzon, V., Salvatella, X. & Méndez, R. CPEB4 is regulated during cell cycle by ERK2/Cdk1-mediated phosphorylation and its assembly into liquid-like droplets. *eLife* **5**, e19298 (2016).
12. Tsang, B., Pritišanac, I., Scherer, S. W., Moses, A. M. & Forman-Kay, J. D. Phase separation as a missing mechanism for interpretation of disease mutations. *Cell* **183**, 1742–1756 (2020).
13. Shin, J., Salameh, J. S. & Richter, J. D. Impaired neurodevelopment by the low complexity domain of CPEB4 reveals a convergent pathway with neurodegeneration. *Sci. Rep.* **6**, 29395 (2016).
14. Marzinke, M. A. & Clagett-Dame, M. The all-trans retinoic acid (atRA)-regulated gene calmin (*Clmn*) regulates cell cycle exit and neurite outgrowth in murine neuroblastoma (Neuro2a) cells. *Exp. Cell. Res.* **318**, 85–93 (2012).
15. Du, L. & Richter, J. D. Activity-dependent polyadenylation in neurons. *RNA* **11**, 1340–1347 (2005).
16. Dreier, J. P. & Reiffurth, C. The stroke–migraine depolarization continuum. *Neuron* **86**, 902–922 (2015).
17. Chesler, M. Regulation and modulation of pH in the brain. *Physiol. Rev.* **83**, 1183–1221 (2003).
18. Martin, E. W. et al. Valence and patterning of aromatic residues determine the phase behavior of prion-like domains. *Science* **367**, 694–699 (2020).
19. Vernon, R. M. et al. Pi–pi contacts are an overlooked protein feature relevant to phase separation. *eLife* **7**, e31486 (2018).
20. Christou-Kent, M. et al. CEBPA phase separation links transcriptional activity and 3D chromatin hubs. *Cell Rep.* **42**, 112897 (2023).
21. Basu, S. et al. Rational optimization of a transcription factor activation domain inhibitor. *Nat. Struct. Mol. Biol.* **30**, 1958–1969 (2023).
22. Tesei, G., Schulze, T. K., Crehuet, R. & Lindorff-Larsen, K. Accurate model of liquid–liquid phase behavior of intrinsically disordered proteins from optimization of single-chain properties. *Proc. Natl Acad. Sci. USA* **118**, e2111696118 (2021).
23. Tesei, G. & Lindorff-Larsen, K. Improved predictions of phase behaviour of intrinsically disordered proteins by tuning the interaction range. *Open Res. Eur.* **2**, 94 (2023).
24. Martin, E. W. & Mittag, T. Relationship of sequence and phase separation in protein low-complexity regions. *Biochemistry* **57**, 2478–2487 (2018).
25. Hervas, R. et al. Cryo-EM structure of a neuronal functional amyloid implicated in memory persistence in *Drosophila*. *Science* **367**, 1230–1234 (2020).
26. Mathieu, C., Pappu, R. V. & Taylor, J. P. Beyond aggregation: pathological phase transitions in neurodegenerative disease. *Science* **370**, 56–60 (2020).
27. Farag, M., Borcherds, W. M., Bremer, A., Mittag, T. & Pappu, R. V. Phase separation of protein mixtures is driven by the interplay of homotypic and heterotypic interactions. *Nat. Commun.* **14**, 5527 (2023).
28. Boyko, S., Surewicz, K. & Surewicz, W. K. Regulatory mechanisms of tau protein fibrillation under the conditions of liquid–liquid phase separation. *Proc. Natl Acad. Sci. USA* **117**, 31882–31890 (2020).
29. Patel, A. et al. A liquid-to-solid phase transition of the ALS protein FUS accelerated by disease mutation. *Cell* **162**, 1066–1077 (2015).
30. Sanfeliu-Cerdán, N. et al. A MEC-2/stomatin condensate liquid-to-solid phase transition controls neuronal mechanotransduction during touch sensing. *Nat. Cell Biol.* https://doi.org/10.1038/s41556-023-01247-0 (2023).
31. Peskett, T. R. et al. A liquid to solid phase transition underlying pathological huntingtin exon1 aggregation. *Mol. Cell* **70**, 588–601.e6 (2018).
32. Molliex, A. et al. Phase separation by low complexity domains promotes stress granule assembly and drives pathological fibrillization. *Cell* **163**, 123–133 (2015).
33. Das, T. et al. Metastable condensates suppress conversion to amyloid fibrils. Preprint at *bioRxiv* https://doi.org/10.1101/2024.02.28.582569 (2024).
34. Mackay, J. A., Callahan, D. J., Fitzgerald, K. N. & Chilkoti, A. Quantitative model of the phase behavior of recombinant pH-responsive elastin-like polypeptides. *Biomacromolecules* **11**, 2873–2879 (2010).
35. Callahan, D. J. et al. Triple stimulus-responsive polypeptide nanoparticles that enhance intratumoral spatial distribution. *Nano Lett.* **12**, 2165–2170 (2012).
36. Quiroz, F. G. et al. Liquid–liquid phase separation drives skin barrier formation. *Science* **367**, eaax9554 (2020).
37. Franzmann, T. M. et al. Phase separation of a yeast prion protein promotes cellular fitness. *Science* **359**, eaao5654 (2018).
38. Picó, S. et al. CPEB alteration and aberrant transcriptome–polyadenylation lead to a treatable SLC19A3 deficiency in Huntington's disease. *Sci. Transl. Med.* **13**, eabe7104 (2021).
39. Parras, A. et al. Polyadenylation of mRNA as a novel regulatory mechanism of gene expression in temporal lobe epilepsy. *Brain* **143**, 2139–2153 (2020).
40. Wang, X.-P. & Cooper, N. G. F. Comparative in silico analyses of *Cpeb1–4* with functional predictions. *Bioinform. Biol. Insights* **4**, 61–83 (2010).
41. Garcia-Cabau, C. & Salvatella, X. Regulation of biomolecular condensate dynamics by signaling. *Curr. Opin. Cell Biol.* **69**, 111–119 (2021).
42. Batlle, C. et al. hnRNPDL phase separation is regulated by alternative splicing and disease-causing mutations accelerate its aggregation. *Cell Rep.* **30**, 1117–1128.e5 (2020).
43. Kjer-Hansen, P. & Weatheritt, R. J. The function of alternative splicing in the proteome: rewiring protein interactomes to put old functions into new contexts. *Nat. Struct. Mol. Biol.* **30**, 1844–1856 (2023).
44. Biesaga, M., Frigolé-Vivas, M. & Salvatella, X. Intrinsically disordered proteins and biomolecular condensates as drug targets. *Curr. Opin. Chem. Biol.* **62**, 90–100 (2021).

Methods

Animals

Cpeb4 KO mice[45] and conditional transgenic mice overexpressing the human CPEB4 isoform that lacks exon 4 (TgCPEB4Δ4)[2] both in a C57BL/6J background were used. All mice were bred and housed in the CBMSO animal facility. Mice were grouped four per cage with food and water available ad libitum and maintained in a temperature-controlled environment on a 12–12 h light–dark cycle with light onset at 8:00 and a relative humidity of 55 ± 10%. Animal housing and maintenance protocols followed local authority guidelines. Animal experiments were performed under protocols approved by the CBMSO Animal Care and Utilization Committee (Comité de Ética de Experimentación Animal del CBMSO, CEEA-CBMSO) and Comunidad de Madrid (PROEX 247.1/20).

Generation of mEGFP–CPEB4 mice

A synthetic sequence consisting of the mEGFP linker sequence flanked by short regions of 5′ homologous (238 bp) and 3′ homologous (99 bp) DNA was obtained (Twist Bioscience). PCR was carried out on the synthetic sequence using the following primers: Fw ssDNA-mGFP–CPEB4 (phosphorylated) tacttcaagcaaacatatttgagatacagggga; Rv ssDNA-mGFP–CPEB4 (thiol-protected) GGTGATGGTGTGGAGGCTGC. Single-stranded DNA (ssDNA) was generated from double-stranded DNA by lambda exonuclease digestion of the phosphorylated strand, followed by gel purification and column extraction. Animals were generated by electroporation of isolated mouse zygotes with ssDNA combined with Cas9 protein and guide/tracr RNA ribonuclear protein complexes (guide; C45gRNA ATCCTAAAAATAATAAATGG). The correct integration of the knock-in cassette was confirmed by PCR and sequencing of the region. The resulting positive mice were crossed with C57BL6/J mice to confirm germline transmission. The offspring were maintained in a C57BL/6J background, and routine genotyping was performed by PCR using the following genotyping primers: 5′-ACGTAGGGTGATAAGCTGTGAT-3′ (Fw) and 5′-AGGGTCTTGTTGTTCTTGCTGT-3′ (Rv). Mice were maintained in a specific pathogen-free facility with a 12–12 h light–dark cycle at 21 ± 1 °C at a relative humidity of 55 ± 10% and given ad libitum access to standard diet and water. Animal handling and all experimental protocols were approved by the Animal Ethics Committee at the Barcelona Science Park and by the Government of Catalonia.

Mouse mEGFP–CPEB4 striatal neuron extraction and culture

mEGFP–CPEB4 mice over 6 weeks of age were crossed in timed matings. Females were weighed weekly to monitor gestation progression. Females with an increment over 3 g up to 18 days after a positive plug were euthanized and embryos were collected at embryonic day 18.5 in cold buffer containing 1× HBSS, 10 mM glucose and 10 mM HEPES. A tail sample was also collected for embryo genotyping. Brains were dissected in the aforementioned buffer on an ice-cold plate, and the striatum was extracted and chopped. Samples were centrifuged and digested with a previously heated solution containing 1× HBSS, 10 mM glucose, 10 mM HEPES, 12 U ml^{-1} papain (Worthington LS003180) and 5 mM L-cysteine for 15 min at 37 °C. Samples were then disaggregated in a buffer containing 1× DMEM/F-12, 2 mM glutamine, 1 mM sodium pyruvate, 20 mM glucose and 10% inactivated horse serum. Cells were seeded at a confluence of 25,000 cells per well in µ-Slide 8-well ibiTreat imaging plates (Ibidi, 80826) previously coated with poly-D-lysine. Cells were then incubated at 37 °C for 1 h. After this time, medium was exchanged with previously tempered medium containing 1× Neurobasal (Gibco, 21103049), 1× B27 with vitamin A (Gibco, 17504044), 2 mM glutamine and 0.5% penicillin–streptomycin (PS). Medium was refreshed every 2–3 days. Neurons were considered differentiated after 7 days of culture. After genotyping, homozygous mEGFP–CPEB4 mice and wild-type littermates were selected for imaging. When specified, cell depolarization was induced by the addition of 50 mM KCl with 1:3 medium dilution. Neurons were maintained in culture for up to 14 days.

mEGFP–CPEB4 distribution in neurons

Primary striatal neurons from mEGFP–CPEB4 mice were imaged at 7 days of differentiation using a LIPSI spinning disk microscope (Nikon). Image acquisition was performed using a fully incubated, high-content, high-speed screening LIPSI platform (Nikon) equipped with an Eclipse Ti2 inverted microscope and a Yokogawa W1 confocal spinning disk unit. The spinning disk unit with an Apo LWD ×40 water lens of 1.15 numerical aperture, and a 488 nm (20%) laser was used for acquisition on a Prime BSI Photometrics sCMOS camera. NIS Elements AR (v.5.30.05) software was used for acquisition, and Fiji/ImageJ software was used to adjust images for visualization.

mEGFP–CPEB4 neuronal stimulation with NMDA

Primary striatal neurons from mEGFP–CPEB4 mice were imaged at 14–21 days of differentiation, and where specified, neuron stimulation was induced by the addition of 20 µM NMDA (Tocris, 0114), a selective NMDA receptor agonist. Stimulated neurons were imaged using a fully incubated Zeiss Elyra PS1 LSM 880 confocal microscope with a Plan ApoChromat ×63/1.2 Imm corr oil objective. A 488 nm (50%) laser was used for acquisition on a Prime BSI Photometrics sCMOS camera. Images were captured every 15 min over the recording period. Zen Elements AR (v.5.30.05) software was used for acquisition, and Fiji/ImageJ software was used for image quantification and to adjust images for visualization. A tailor-made macro applying an intensity threshold was used to accurately segment cytoplasmic condensates and the whole cell for each time frame. The condensed fraction per frame was obtained as the sum of areas of condensates divided by the cell area. For representation, the values were normalized to that measured at the end of the stimulation period.

nCPEB4 extraction from mouse brains

To extract nCPEB4 from the brains of 6-month-old control mice, *Cpeb4* KO mice and TgCPEB4Δ4 mice, around 500 mg of tissue was first collected and snap-frozen in liquid nitrogen. Each sample was homogenized in 5 ml lysis buffer (50 mM Tris, pH 7.7, 5% glycerol, 0.1% Triton X-100, 1% NP-40, 50 mM NaCl, 50 mM imidazole and Pierce protease inhibitor, EDTA-free) using a Polytron homogenizer and rotated for 30 min at 4 °C. The homogenate was moved to high-speed PPCO centrifuge tubes and centrifuged at 48,000*g* at 4 °C for 20 min. After this, the supernatant was retained while the resultant pellet was dissolved in 4 ml lysis buffer and homogenized further using the Polytron homogenizer with the same protocol. This process was repeated 3 times (with 1 ml reduction of lysis buffer after each round of homogenization) to maximize the extraction of nCPEB4. To further clarify the combined supernatants, they were filtered through a Miracloth membrane (Millipore) to remove lipids and then passed through a 0.45 µm filter. Exploiting the histidine-rich regions present in the sequence of nCPEB4 (^{23}RFHPHLQPPHHHQN^{36} and ^{229}LSQHHPHHPHFQHHHSQHQQ^{248}), a 2-elution step Ni^{2+}-affinity chromatography was carried out using a Histrap HP 5 ml (GE Healthcare) on a FPLC apparatus (ÄKTA Pure, GE Healthcare). The combined supernatants were injected into a column pre-equilibrated with binding buffer consisting of 50 mM Tris, pH 7.7, 50 mM NaCl and 50 mM imidazole. The bound fraction was initially washed in a high-salt buffer consisting of 50 mM Tris, pH 7.7, 1 M NaCl and 50 mM imidazole. This step is crucial as it removes a high-molecular-weight nonspecific binder that was detectable by western blotting (WB), even in the *Cpeb4* KO mice. The removal of this nonspecific binder is important to ensure the integrity of subsequent analyses. Once the nonspecific binder was completely removed, nCPEB4 was eluted using a second buffer containing 50 mM Tris, pH 7.7, 50 mM NaCl and 500 mM imidazole. The non-bound, washed and eluted fractions were then analysed by WB using Bis-Tris 4–12% gradient gels. At this point, fractions containing

nCPEB4, verified by WB in SDS–PAGE, were used for proteinase K digestion and SDS-resistance analysis using 1.5% SDD–AGE as previously described[46]. Here, the non-boiling proteins were transferred to a nitrocellulose membrane by capillary methods and probed with an anti-CPEB4 antibody. Samples identified as CPEB4 monomers and aggregates were selected for subsequent seeded aggregation assay. Additionally, to quantify the amount of CPEB4 aggregates, the same samples were injected into a Superdex 200 Increase 10/300 GL (GE Healthcare) column pre-equilibrated with 1× PBS, pH 7.5. The eluted fractions from the gel filtration chromatography were combined every 4 fractions (2 ml) and concentrated into 100 µl using a Pierce concentrator, PES, 30 K MWCO, 0.5 ml, to be ultimately analysed using 1.5% SDD–AGE. For all the blots described here, including SDS–PAGE, immunodot blots and SDD–AGE, a 1:2,000 dilution of polyclonal rabbit anti-CPEB4 antibody (Abcam, ab224162) and a 1:5,000 dilution of HRP-linked anti-rabbit IgG antibody (Cell Signaling Technology, CST-7074S) were used.

Proteinase K digestion

About 400 ng of total protein, estimated from BCA assays, containing endogenous nCPEB4 extracted from the brains of 6-month-old control mice, *Cpeb4* KO mice and TgCPEB4Δ4 mice were digested with 0.1, 0.5, 1, 5 and 10 ng of proteinase K for 2 min at 37 °C. Proteinase K activity was stopped by heating the samples to 75 °C. Next, 2 µl of the enzyme-treated reaction mixture was manually applied to a nitrocellulose membrane. The membrane was blocked in 5% milk in TBS-T buffer and probed with anti-CPEB4 antibody (Abcam, ab224162).

Seeded aggregation assay

A concentration of 1% w/w of the seed, 40 ng of total protein containing nCPEB4 aggregates extracted from TgCPEB4Δ4 mouse brains, was incubated with the substrate, which consisted of 4 µg total protein containing soluble nCPEB4 extracted from wild-type (WT) mouse brains. Unless concentrated 100-fold, the seed used was not detectable by WB. The seeding reaction was carried out at 4 °C for 24 h during the time course experiment in 50 mM Tris, pH 7.7, and 50 mM NaCl. The seeded reactions, which were non-boiled, were analysed using 1.5% SDD–AGE as previously described[46]. The proteins were transferred to a nitrocellulose membrane by capillary methods and probed with anti-CPEB4 antibody (Abcam, ab224162) to follow the aggregation of WT nCPEB4 in a time-dependent manner.

Proteostat staining and CPEB4 immunofluorescence

Six-week-old TgCPEB4Δ4 mice ($n = 4$) and control littermates ($n = 3$) were anaesthetized by an intraperitoneal injection of pentobarbital and then transcardially perfused with PBS. Brains were immediately removed and each hemisphere placed in 4% paraformaldehyde overnight at 4 °C, followed by 3 PBS washes (10 min each) and then immersed in 30% sucrose in PBS for 72 h at 4 °C and them included in optimum cutting temperature compound (Tissue-Tek, Sakura Finetek Europe, 4583) and immediately frozen. Samples were stored at −80 °C until use.

Brain hemispheres were cut sagittally at 30 µm on a cryostat (Thermo Scientific), and sections were stored (free floating) in glycol-containing buffer (30% glycerol and 30% ethylene glycol in 0.02 M PB) at −20 °C.

For staining, sections (2 per mouse) were washed in PBS to eliminate the cryoprotective buffer and permeabilized in 0.2% Triton X-100 for 30 min at room temperature, and then stained with the dye Proteostat (Enzo51035-K100; 1:2,000) for 15 min at room temperature followed by 2 PBS washes (10 min each) and then 1% acetic acid for 30 min at room temperature, followed by 3 PBS washes (10 min each). For CPEB4 immunofluorescence, sections were immersed in blocking solution (2% NGS, 1% BSA and 0.2% Triton X-100 in PBS) for 1 h at room temperature and then incubated overnight at 4 °C with anti-CPEB4 primary monoclonal antibody (1:1,000, mouse monoclonal, homemade, ERE149C) in blocking solution. After 3 PBS washes (10 min each), sections were incubated with Alexa 488 donkey anti-mouse secondary antibody (1:500, Thermo Fisher, A-21202) for 1 h followed by 3 PBS washes (10 min each) and, finally, nuclei were stained by incubating with DAPI (1:10,000 in PBS, Merck) followed by 3 PBS washes (10 min each) and mounted with Prolong medium (Life Technologies).

Images of the striatum were obtained with a vertical Axio Observer. Z1/7 laser scanning microscope (LSM 800, Carl Zeiss) at ×63 magnification with ×2 optical zoom and analysed by performing *z* stacks (11 optical sections with a thickness of 1 µm, spanning 6.6 µm on the *z* axis). Sequential scanning mode was used to avoid crosstalk.

Medium-sized spiny neurons were distinguished by the morphology and size of the nucleus, and fields were selected to typically include 4–8 medium-sized spiny neurons. The number of Protesotat and CPEB4 double-positive foci was manually counted per cell fully included within the *z* stack. Typically, between 16 and 20 cells were analysed per mouse from a total of 50 control and 73 TgCPEB4Δ4 neurons.

Significance for differences in the number of positive foci between control mice and TgCPEB4Δ4 mice was assessed using a generalized linear mixed model (family = Poisson(link = 'identity')) with mouse as the random effect (Supplementary Methods).

Plasmids for expression in N2a cells

Human nCPEB4 (UniProt identifier Q17RY0-1) FL open reading frame (ORF) was cloned into a pBSK vector. The me4 sequence (nucleotides 1258–1281) was deleted by PCR on a pBSK-nCPEB4 plasmid using Gibson assembly master mix (New England Biolabs, E2611S) following the manufacturer's instructions. Mutagenesis of nCPEB4 phosphorylation sites was performed using a QuikChange Lightning Multi Site-Directed Mutagenesis kit (Agilent Technologies, 210513), with oligonucleotides purchased from Sigma-Aldrich, following the manufacturer's instructions. ΔHC mutants were generated by PCR mutagenesis on a pBSK-nCPEB4 plasmid, with oligonucleotides purchased from Sigma-Aldrich. For cell transfection, nCPEB4 ORF, FL, NTD and mutants were cloned into pPEU4 and pPEU5 vectors, which contain a C-terminal eGFP or mCherry tag, respectively, by In-Fusion (BD Clontech) cloning reaction[47]. For BioID, xCPEB4 or BirA ORF was cloned into a pBSK vector. me4 was added to the xCPEB4 sequence by PCR on a pBSK-xCPEB4 plasmid using Gibson assembly master mix (New England Biolabs, E2611S) and following the manufacturer's instructions. A MYC tag and BirA ORF were added at the N terminus of pBSK-xCPEB4 plasmid. For competition experiments, xCPEB1 RRMZZ and xCPEB4 RRM domains were cloned in pBSK, and a HA tag was added at the N terminus. pBSK-Emi2 3′ UTR was obtained from a previous study[48].

N2a cell culture, differentiation and DNA transient transfection

N2a cells were grown in DMEM with 10% FBS, 1% PS and 2 mM L-glutamine for maintenance. For fixed-cell imaging, cells were seeded on 6-well plates with 12-mm-diameter poly-lysine-coated glass coverslips (Marienfeld Superior). For live-cell imaging, cells were seeded on µ-Slide 8-well ibiTreat plates. For differentiation, medium was exchanged with DMEM with 0.5% FBS, 1% PS, 2 mM L-glutamine and 1 µM retinoic acid and cells were grown for 48 h. They were then transfected at 60% confluence with 1.25 µg DNA using Lipofectamine LTX and Plus reagent (Thermo Fisher, 15338100) following the manufacturer's protocol. When specified, N2a depolarization was induced as described for striatal neurons, specified in the section 'Mouse mEGFP–CPEB4 striatal neuron extraction and culture'.

N2a cell line characterization

N2a cells, like neurons, express CPEB4 variants including and excluding me4 (nCPEB4 and nCPEB4Δ4, respectively), independently of their differentiation status (Extended Data Fig. 1e). By contrast, cell lines of non-neural origin only express nCPEB4Δ4. Inclusion of me4 in N2a cells correlates with the expression of the splicing factor SRRM4 but not with that of RBFOX1 (Extended Data Fig. 1f). Depletion of SRRM4 in N2a cells

decreases the inclusion of me4, whereas overexpression of SRRM4 in the non-neuronal cell line 293T forces its inclusion[5,49] (Extended Data Fig. 1g). N2a cells, therefore, recapitulate the neuron-specific regulation of CPEB4 alternative splicing.

nCPEB4–GFP distribution in N2a cells

Twenty-four hours after transfection, N2a cells were fixed with 4% paraformaldehyde (Aname, 15710) in PBS for 10 min at room temperature. They were then washed with PBS and incubated with 0.5 µg µl^{-1} DAPI (Sigma) for 15 min. Coverslips were rinsed with PBS and mounted on a glass slide with Prolong Gold Antifade mountant (P36934, Invitrogen). Image acquisition was performed with a Leica SP5 confocal microscope (Leica Microsystems), and *z* series stacks were acquired at 1,024 × 1,024 pixels using a ×63/1.4 numerical aperture oil immersion objective with a zoom factor of 2. Argon 488 nm (20%) and diode 405 nm (10%) lasers were used. Hybrid detectors for GFP (500–550 nm with 33% gain) and DAPI (415–480 nm, 33% gain) were used for acquisition. LAS AF Leica software was used to acquire 10–20 *z* stack slices per cell with a *z* step size of 0.5 µm. Fiji/ImageJ software was used to perform the image analysis. A tailor-made macro using BioVoxxel Toolbox and 3D object counter plug-ins was used to accurately segment and obtain the number and volume of foci per cell.

Live-cell imaging of GFP-tagged CPEB4 variants in N2a cells

Live imaging of overexpressed nCPEB4–GFP variants in N2a cells was performed 20 h after transfection, whereas primary striatal neurons from mEGFP–CPEB4 mice were imaged at 7 days of differentiation. For both types of cells, image acquisition was performed using a spinning disk microscope (Andor Revolution xD, Andor). A total of 24 images were taken per experiment (4 before the addition of the stimulus and 20 after), with 13 *z* stacks at 512 × 512 pixels of format resolution. Images were acquired with a step size of 0.5 µm. For acquisition, the typical frame rate was adjusted to 5 images per s at 50 ms integration time of the EMCCD camera (Andor). An argon 488 nm laser (20%) was used for acquisition with a 1.4 numerical aperture/×60 oil immersion objective. Fiji/ImageJ software was used to obtain a *z* projection of the *z* stacks and subsequent concatenation of images. The obtained time-lapse images were subsequently used for manual quantification of nCPEB4 dissolution events. Cells were manually classified into two categories depending on the existence of cytoplasmic foci at $t = 60$ min: cells with remaining foci or cells without. For nCPEB4 and nCPEB4Δ4 FL comparison, the percentage of cells with remaining cytoplasmic foci after the depolarizing stimuli ($t = 60$ min) was calculated from a pool of 7 experiments. Unless specified, the percentage of cells with remaining cytoplasmic foci after the depolarizing stimuli ($t = 60$ min) was calculated per each experiment. When specified, blind analysis and classification were performed independently by a group of four different people from a pool of experiments.

FRAP in N2a cells

A spinning disk microscope from Andor, equipped with a FRAPPA module, was used for FRAP experiments. A total of 350 images were taken per experiment (50 images before the bleaching and 300 after) at 512 × 512 pixels. The typical frame rate was set to the fastest (88 ms) with an exposure time of 50 ms on an EMCCD camera. An AOTF 488 nm laser (20%) was used for acquisition, and 50% laser intensity was set for bleaching in 2 repeats with a dwell time of 40 ms. Fiji/ImageJ software was used for FRAP analysis. Three regions of interest (ROIs) were defined per video: background, cell and bleaching area. The mean fluorescence intensity was obtained for the 3 ROIs for all 350 frames, and the output was exported in tabular format. Outputs were then entered on the easyFRAP website[50]. Full-scale normalization was selected, 'initial values to discard' was set to 20 and the curves obtained were fitted to a single exponential model. Fluorescence recovery curves, mobile fraction and half time of recovery were obtained for each experimental condition.

Mapping of nCPEB4 post-translational modified sites by mass spectrometry

Overexpressed nCPEB4–GFP and nCPEB4Δ4–GFP were immunoprecipitated from basal (–stim) and stimulated (+stim) N2a differentiated cells. Cells were lysed in ice-cold RIPA buffer containing 50 mM Tris HCl pH 8, 1% Nonidet P-40 (NP40), 0.1% SDS, 1 mM EDTA, 150 mM NaCl, 1 mM $MgCl_2$, 1× EDTA-free complete protease inhibitor cocktail (Roche, 5056489001) and phosphatase inhibitor cocktails (Sigma, P5726 and P0044). Cells were subsequently sonicated for 5 min at low intensity with a standard bioruptor diagenode. Following centrifugation (4 °C for 10 min at maximum speed), supernatants were collected, precleared and immunoprecipitated overnight at 4 °C with 50 µl GFP-conjugated Dynabeads protein A (Invitrogen). Beads had previously been conjugated with 5 µl anti-GFP antibody (Invitrogen, A6455) diluted in 500 µl PBS 1× for 2 h at room temperature. After immunoprecipitation, beads were washed with cold RIPA buffer and eluted with Laemmli sample buffer. Eppendorf LoBind microcentrifuge tubes (Eppendorf, 30108116) were used for the entire protocol. The immunoprecipitated elutions were run on precast 4–20% gradient gels (Midi Criterion TGX, Bio-Rad) and stained with Coomassie blue for 1 h at room temperature. Bands at the expected nCPEB4–GFP molecular weight were cut, washed with 50 mM NH_4HCO_3 and acetonitrile, reduced with 10 mM DTT and alkylated with 50 mM IAA. Samples were digested with trypsin and digestion was stopped by the addition of 5% formic acid. Following evaporation, samples were reconstituted in 15 µl of 1% formic acid and 3% acetonitrile. Mass spectrometry analysis of nCPEB4 PTM sites was performed as previously described[7] with some modifications. In brief, samples were loaded in a µ-precolumn at a flow rate of 250 nl min^{-1} using Dionex Ultimate 3000. Peptides were separated using a NanoEase MZ HSS T3 analytical column with a 60 min run and eluted with a linear gradient from 3 to 35% buffer B in 60 min (buffer A: 0.1% formic acid in H_2O; buffer B: 0.1% formic acid in acetonitrile). The column outlet was directly connected to an Advion TriVersa NanoMate (Advion) fitted on an Orbitrap Fusion Lumos Tribrid (Thermo Scientific). Spray voltage in the NanoMate source was set to 1.7 kV. The mass spectrometer was operated in a data-dependent acquisition mode. Survey mass spectrometry scans were acquired in the orbitrap with the resolution (defined at 200 *m/z*) set to 120,000. The top speed (most intense) ions per scan were fragmented in the HCD cell and detected in the orbitrap.

For peptide identification, searches were performed using MaxQuant (v.1.6.17.0) software and run against a target and decoy database to determine the false discovery rate. The database included proteins of interest sequences (nCPEB4–GFP and nCPEB4Δ4–GFP) and contaminants. Search parameters included trypsin enzyme specificity, allowing for two missed cleavage sites, oxidation in methionine, phosphorylation in serine, threonine and tyrosine, methylation and demethylation in lysine and arginine, and acetylation in the protein N terminus as dynamic modifications, and carbamidomethyl in cysteine as a static modification. Peptides with a *q* value lower than 0.1 and false discovery rate < 1% were considered as positive identifications with a high confidence level. Mass spectrometry spectra were searched against contaminants (released in 2017) and user proteins using Andromeda and MaxQuant (v.1.6.17.0) software. To accept a site as modified, PTM localization probability was set above 75%. For the differential expression analysis, a *t*-test on PTM site intensities from MaxQuant was applied for each site within nCPEB4 variants. For data visualization, two parameters were used for each PTM site, namely the sum of intensities of modified peptides that contain the specific PTM-site (Int_mod) and the PTM-to-base ratio, with the latter calculated as: Int_mod/Int_unmod, where Int_unmod is the sum of intensities of unmodified peptides that contain the site. For data visualization, the PTM-to-total ratio was calculated for each site as follows: PTM-to-total = Int_mod/(Int_mod + (Int_mod/PTM-to-base)).

Effect of phosphorylations on condensate dissolution

To strengthen the conclusion that phosphorylation of nCPEB4 does not promote condensate dissolution, we studied the behaviour in N2a cells of the condensates formed by phosphomimicking (S/T to D) and non-phosphorylatable (S/T to A) variants of nCPEB4(NTD), the phosphorylation status of which cannot be altered by depolarization. In agreement with our previous findings[11], the former had a lower propensity to condense (Extended Data Fig. 2c) and, in agreement with our conclusion, both variants dissolved after depolarization (Extended Data Fig. 2d,e).

Intracellular pH tracking

Quantitative determination of intracellular pH (pH_i) was performed using the cell-permeant ratiometric pH indicator SNARF-5F 5-(and-6)-carboxylic acid AM (Thermo Fisher) in live imaged N2a cells at 48 h of differentiation. In brief, for loading the pH indicator into cells, they were incubated with 10 µM SNARF-5F 5-(and-6)-carboxylic acid AM diluted in serum-free DMEM for 15 min at 37 °C. Cells were then washed and imaged in serum-free DMEM. A Zeiss Elyra PS1 LSM 880 confocal microscope using a Plan ApoChromat ×40/1.2 Imm corr DIC M27 water objective was used for acquisition at 2 emission wavelengths: ~575 nm and 640 nm. Images were captured every 30 s over the recording period. pH_i estimation was performed as described in previous publications[51]. In brief, in vivo pH_i calibration was performed by fixing the pH_i between 5.5 and 7.5 with a commercially available intracellular pH calibration buffer kit (Thermo Fisher). Valinomycin and nigericin were used to equilibrate the intracellular pH. The intensity of fluorescence emitted at the two wavelengths was used to calculate a ratio ($R_{F640/F575}$) that is proportional to pH_i. Fluorescence ratio values ($R_{F640/F575}$) from cells with fixed pH_i were used to obtain a calibration curve for each biological replicate. Experimental pH_i estimation from the fluorescence ratio values was calculated using the following equation: $pH_i = (R_{F640}/F_{575} + b)/m$, where m is the slope from the calibration curve equation and b is the intercept.

RNA extraction and real-time quantitative RT–PCR

For N2a RNA extraction, cells were scraped into an ice-cold plate, collected and centrifuged at 500*g* for 5 min at 4 °C. For mouse tissue RNA extraction, organs were ground with a liquid-nitrogen-cooled mortar to obtain tissue powder. Total RNA was extracted from both cells and tissue powder using TRIsure reagent (Bioline, Ecogen, BIO-38033) following the manufacturer's protocol and using phenol–chloroform. The RNA concentration was determined using a Nanodrop spectrophotometer (Nanodrop Technologies). Next, 1 µg of total RNA was reverse transcribed using RevertAid reverse transcriptase (Themo Fisher, EP0442) following the manufacturer's recommendations and using oligodT and random hexamers as primers. Quantitative real-time PCR (qPCR) was performed in triplicate in a QuantStudio 6flex (Thermo Fisher) using PowerUp SYBR green master mix (Thermo Fisher, A25778). All quantifications of mRNA levels were first normalized to an endogenous housekeeping control (*Tbp*), and then mRNA relative quantities to a reference sample (brain, N2a undifferentiated) were calculated using the 2–ΔΔCt method. The following primers were used for qPCR: 5′-TGATTCCATTAAAGGTCGTCTAAACT-3′ (Fw) and 5′-GAAACAATGAAGACTGACCTCTCCTT-3′ (Rv) for Mm *Cpeb4* isoform containing exons 3 and 4; 5′-TGATTCCATTAAAGCAAGGACTTATG-3′ (Fw) and 5′-GCTGTGATCTCATCTTCATCAATATC-3′ (Rv) for Mm *Cpeb4* isoform lacking exon 3; 5′-TGATTCCATTAAAGGTCGTCTAAACT-3′ (Fw) and 5′-GGAAACAATGAAGACTGACCATTAAT-3′ (Rv) for Mm *Cpeb4* isoform lacking exon 4; 5′-ATTCCATTAAAGGTCAGTCTTCATTG-3′ (Fw) and 5′-GCTGTGATCTCATCTTCATCAATATC-3′ (Rv) for Mm *Cpeb4* isoform lacking exons 3 and 4; 5′-GGAAAGGGACCTTCAAAGCAGT-3′ (Fw) and 5′ CTCTGTCCTTGGCATCGGCT-3′ (Rv) for Mm *Srrm4*; and 5′-ACTTCTAT GCAGGCACGGTG-3′ (Fw) and 5′-AGCCAGGCATTGCAGAAGTAT-3′ (Rv) for Mm *Rbfox1*. Mm JunB and cFos primers were obtained from a previous study[5].

Real-time semi-quantitative RT–PCR

For CPEB4 splicing isoform amplification, specific primers were used in CPEB4 exon 2 (Fw primer) and exon 5 (Rv primer) as previously described[2]. PCR products conforming to the 4 isoforms of CPEB4 were resolved on a 2% agarose/GelRed gel run at 130 V for 2 h.

WB analysis

Cells were lysed in ice-cold buffer containing 1% NP40, 150 mM NaCl, 50 mM Tris HCl (pH 7.5), 2 mM EDTA, 2 mM EGTA, 20 mM sodium fluoride, 2 mM PMSF, 2 mM sodium orthovanadate, 1 mM DTT and 1× EDTA-free complete protease inhibitor cocktail. Lysed samples were then sonicated at medium intensity for 5 min with a standard bioruptor diagenode, and total protein content was quantified using a DC Protein assay (Bio-Rad, 5000113). Next, 15–30 µg of total protein lysate was resolved on SDS–PAGE gels and transferred to a nitrocellulose membrane (Cytiva, 10600001). After 1 h of blocking at room temperature in 5% non-fat milk, membranes were incubated overnight at 4 °C with primary antibodies and subsequently with secondary antibodies for 2 h at room temperature. Specific proteins were labelled using the following primary antibodies: CPEB4 (1:100, homemade, mouse monoclonal, ERE149C); GFP (1:2,000, Invitrogen, rabbit polyclonal, A6455); MYC (1:1,000, Abcam, goat polyclonal, ab9132); and β-actin (1:10,000, Abcam, mouse monoclonal, ab20272) or streptavidin (1:5,000, Thermo Fisher, S911). The following secondary antibodies were used: goat anti-mouse (1:300, Thermo Fisher, 31430); goat anti-rabbit (1:300, Thermo Fisher, G-21234); and donkey anti-goat (1:300, Abcam, ab6885). Membranes were then incubated for 3 min with Amersham ECL TM WB detection reagents (Sigma, GERPN2106) or for 5 min with Clarity Western ECL substrate (Bio-Rad, 1705061).

nCPEB4 and nCPEB4Δ4 co-localization experiments in N2a cells

mCherry red signals were acquired with a DPSS 561 excitation laser (9%) and a HyD2 detector set to 570–650 nm with a gain of 33%. DAPI and GFP signals were acquired using the settings specified in the section 'nCPEB4–GFP distribution in N2a cells'. For measuring the extent of co-localization between the two channels, the ImageJ JaCoP plug-in was used to obtain Pearson's correlation coefficients and Mander's overlap coefficients per cell.

Immunohistochemistry

Mouse embryos at embryonic day 13.5 were fixed in 10% neutral-buffered formalin solution and embedded in paraffin. Rabbit polyclonal primary antibody anti-CPEB4 (Abcam, ab83009) was used at 1:1,000 dilution. Embryo sections were counterstained with haematoxylin.

X. laevis oocyte preparation

Stage VI oocytes were obtained from full-grown *X. laevis* females as previously described[52]. In brief, ovaries were treated with collagenase (2 mg ml^{-1}; StemCell Technologies) and incubated in modified bath saline 1× medium with 0.7 mM $CaCl_2$. Animal handling and all experimental protocols were approved by the Animal Ethics Committee at the Barcelona Science Park and by the Government of Catalonia.

X. laevis BioID

BioID was performed as previously described[7]. In brief, 150 stage VI *X. laevis* oocytes were microinjected with 50.6 nl of 50 ng $µl^{-1}$ in vitro transcribed and polyadenylated RNAs corresponding to MYC-BirA-xCPEB4 variants. Oocytes were then incubated in 20 µM biotin (Merck) at 18 °C for 40 h. Oocytes were lysed in cold lysis buffer and centrifuged twice at 16,000*g* at 4 °C for 15 min. Cold BioID lysis buffer was added to cleared extract, and the resulting mixture was subjected to clearing with PD MiniTrap G-25 columns (GE Healthcare).

Next, 1.6% Triton X-100 and 0.04% SDS were added, and extracts were incubated with MyOne Dynabeads Streptavidin C1 (Invitrogen). The beads were then washed with a subsequent sequence of wash buffers. The beads were resuspended in 3 M urea, 50 mM NH_4HCO_3, pH 8.0, and 5 mM DTT for 1 h at room temperature with orbital shaking and subsequently incubated in 10 mM iodoacetamide for 30 min at room temperature, and then DTT was added. Proteins were on-bead digested with trypsin (Promega) at 37 °C for 16 h with orbital shaking. Digestion was stopped by the addition of 1% formic acid. Mass spectrometry analysis of biotinylated proteins in xCPEB4 and xCPEB4 + Ex4 was carried out at the Mass Spectrometry Facility at IRB Barcelona as previously described[7]. In brief, samples were analysed using an Orbitrap Fusion Lumos Tribrid mass spectrometer (Thermo Scientific). The MS/MS spectra obtained were searched against the UniProt (Xenopodinae, release 2017_02) and contaminants databases, and proteins of interest sequences using Proteome Discoverer (v.2.1.0.81).

Identification of the nCPEB4 isoform interactome by immunoprecipitation coupled to mass spectrometry

Overexpressed nCPEB4–GFP, nCPEB4Δ4–GFP and GFP (control) were immunoprecipitated from differentiated N2a cells. Cells were lysed in ice-cold RIPA buffer containing 50 mM Tris HCl pH 8, 1% Nonidet P-40 (NP40), 0.1% SDS, 1 mM EDTA, 150 mM NaCl, 1 mM $MgCl_2$, 1× EDTA-free complete protease inhibitor cocktail (Roche, 5056489001) and phosphatase inhibitor cocktails (Sigma, P5726, and P0044). Cells were subsequently sonicated for 5 min at low intensity with a standard bioruptor diagenode. Following centrifugation (4 °C for 10 min at maximum speed), supernatants were collected, precleared and immunoprecipitated overnight at 4 °C with 50 µl GFP-conjugated Dynabeads protein A (Invitrogen). Beads had previously been conjugated with 10 µl anti-GFP antibody (Invitrogen, A6455) diluted in 500 µl PBS 1× for 2 h at room temperature. After immunoprecipitation, beads were washed with cold RIPA buffer (containing 0.05% NP-40 and 0.1% SDS) and eluted with Laemmli sample buffer. Eppendorf LoBind microcentrifuge tubes (Eppendorf, 30108116) were used for the entire protocol. The immunoprecipitated elutions were shortly run on 8% acrylamide 0.75 mm gels until the whole individual samples were compacted at the upper part of the running gel. Then, gels were stained with InstantBlue Coomassie for 1 h at room temperature. Bands corresponding to elutions were cut, washed and digested with 0.1 µg $µl^{-1}$ trypsin, (Promega). Samples were digested with trypsin and digestion was stopped by the addition of 5% formic acid. Following evaporation, samples were reconstituted in 12 µl of 1% formic acid and 3% acetonitrile. In brief, mass spectrometry analysis of immunoprecipitates was performed as follows: samples were loaded into an Evotip trap column (Evosep) at a flow rate of 250 nl min^{-1}. Peptides were separated using a EV1137 analytical column (Evosep) with a 88-min run and eluted with buffer A (0.1% formic acid in H_2O) and buffer B (0.1% formic acid in acetonitrile). The column outlet was directly connected to an Easyspray (Thermo Scientific) fitted on an Orbitrap Eclipse Tribrid (Thermo Scientific). Spray voltage in the Easyspray source was set to 2.5 kV. The mass spectrometer was operated in data-dependent acquisition mode. The top speed (most intense) ions per scan were fragmented in the HCD cell and detected in the orbitrap. For peptide identification, searches were performed using Proteome Discoverer (v.2.5.0.400) software and run against databases including universal contaminants, mouse from Swissprot (2023/04) and bait proteins. Search parameters included trypsin enzyme specificity, allowing for two missed cleavage sites, oxidation in methionine, acetylation in the protein N terminus, methionine loss in the N terminus, and methionine loss in and acetylation in the N terminus as dynamic modifications, and carbamidomethyl in cysteine as a static modification. Protein hits in co-precipitates from each isoform were determined using a differential analysis of protein abundance in nCPEB4–GFP or nCPEB4Δ4–GFP relative to GFP. Protein group abundance values from Proteome Discoverer were used for protein quantification, and cut-off values for the fold change (|FC| > 1.5) and adjusted *P* value (padj < 0.05) were applied to define over-abundant significant proteins. Significant hits included proteins with no missing values in the three conditions (nCPEB4, nCPEB4Δ4 or GFP) or in only one condition, for which value imputation was performed. Only significant hits were considered for subsequent analyses. Protein hits differentially represented in nCPEB4Δ4–GFP versus nCPEB4–GFP were determined by a differential abundance analysis between the two baits, applying fold change (|FC| > 1.5) and padj < 0.05) as cut-off values.

Competition experiments

Competition experiments were performed as previously described[10] using 23 nl of 500 ng $µl^{-1}$ in vitro transcribed and polyadenylated RNAs encoding for HA-tagged xCPEB1 and xCPEB4 RRMs and variants. Not injected was considered as 0% competition whereas HA-xCPEB1 RRM was considered as 100% competition.

Plasmids for protein expression in *Escherichia coli*

An insert codifying for the nCPEB4(NTD) protein sequence (UniProt identifier Q17RY0-2, residues 1–448) was ordered in GenScript subcloned in a pET-30a(+) vector. The His_6 tag and S tag from the plasmid were removed by PCR using a NEB Q5 site-directed mutagenesis kit, with oligonucleotides purchased from Sigma-Aldrich. The histidine to serine mutants were ordered from GenScript subcloned in a pET-30a(+) vector in the NdeI and XhoI restriction enzymes positions. The nCPEB4Δ4, ΔHC and Δ4ΔHC mutants were generated by PCR mutagenesis on the nCPEB4(NTD) plasmid using a NEB Q5 Site-directed mutagenesis kit, with oligonucleotides purchased from Sigma-Aldrich. The sequences of the N-terminal domain of nCPEB4 and mutants used for the in vitro experiments are described in Supplementary Methods.

Protein expression and purification for in vitro experiments

E. coli B834 cells were transformed with the pET-30a(+) plasmids. For non-isotopically labelled protein, the cells were grown in LB medium at 37 °C until the optical density at 600 nm (OD_{600}) was 0.6, and then the cultures were induced with 1 mM IPTG for 3 h at 37 °C. For ^{15}N or ^{15}N,^{13}C isotopically labelled protein, the cells were grown in LB medium until OD_{600} = 0.6 and then transferred into M9 medium[53] (3 litres LB for 1 litre M9) containing $[^{15}N]H_4Cl$ or $[^{15}N]H_4Cl$ and [^{13}C]glucose, respectively, and then the cultures were induced with 1 mM IPTG overnight at 37 °C. The cultures were then centrifuged for 30 min at 4,000 r.p.m., and the cells were resuspended with lysis buffer (50 mM Tris-HCl, 1 mM DTT, 100 mM NaCl, 0.05% Triton X-100, at pH 8.0, and supplemented with 500 µl of PIC and 500 µl of 100 mM PMSF).

The cells were lysed by sonication and centrifuged for 30 min at 20,000 r.p.m. The pellet was washed first with wash-1 buffer (20 mM Tris-HCl, 1 mM DTT, 1 M NaCl, 0.05% Triton X-100, at pH 8.0, and supplemented with 500 µl of PIC, 500 µl of 100 mM PMSF, and 50 µl of 5 mg ml^{-1} DNAse) and then with wash-2 buffer (20 mM Tris-HCl, 1 mM DTT, 0.1 M L-arginine, at pH 8.0). The pellet was resuspended with the nickel-A buffer (25 mM Tris-HCl, 1 mM DTT, 50 mM NaCl, 8 M urea and 20 mM imidazole, at pH 8.0) and centrifuged for 30 min at 20,000 r.p.m. The supernatant was injected at room temperature into a nickel affinity column and eluted with a gradient from 0 to 100% of nickel-B buffer (25 mM Tris-HCl, 1 mM DTT, 50 mM NaCl, 8 M urea and 500 mM imidazole, at pH 8.0). The fractions with protein were pooled, and 1 mM EDTA was added. The sample was injected into a size exclusion Superdex 200 16/600 (GE Healthcare) column, running at 4 °C in size exclusion buffer (25 mM Tris-HCl, 1 mM DTT, 50 mM NaCl and 2 M urea, at pH 8.0). The fractions with protein were pooled and concentrated to approximately 150 µM. The sample was dialysed against the final buffer (20 mM sodium phosphate, 1 mM TCEP and 0.05% NaN_3, at pH 8.0), fast frozen in liquid nitrogen and stored at −80 °C.

Peptide for in vitro experiments

The me4$(GS)_3$me4 synthetic peptide with amidated or Cy3-modified C terminus and acetylated N terminus was obtained as lyophilized powder with >95% purity from GenScript. The peptide was dissolved in 6 M guanidine thiocyanate and incubated with agitation overnight at 25 °C. The sample was then centrifuged at 15,000 r.p.m. for 10 min. The supernatant was extensively dialysed against the final buffer (20 mM sodium phosphate, 1 mM TCEP and 0.05% NaN_3, at pH 8.0)[54]. The peptide sample was then manipulated in the same way as the protein samples, as detailed below.

Sample preparation for in vitro experiments

All samples were prepared on ice as follows. First, a buffer stock solution consisting of 20 mM sodium phosphate buffer with 1 mM TCEP and 0.05% NaN_3 was pH adjusted to 8.0 (unless otherwise indicated) and filtered using 0.22 µm sterile filters (buffer stock). A 1 M NaCl solution in the same buffer was also pH adjusted to 8.0 (unless otherwise indicated) and filtered (salt stock). The protein samples were then thawed from −80 °C on ice, pH adjusted to 8.0 (unless otherwise indicated) and centrifuged for 5 min at 15,000 r.p.m. at 4 °C. The supernatant (protein stock) was transferred to a new Eppendorf tube, and the protein concentration was determined by measuring its absorbance at 280 nm. The samples were prepared by mixing the correct amounts of buffer stock, protein stock and salt stock, as well as other indicated additives in the experiments, to reach the desired final protein and NaCl concentrations.

Apparent absorbance measurement as a function of temperature

The absorbance of the samples was measured at 350 nm ($A_{350\,nm}$) using 1 cm pathlength cuvettes and a Cary100 ultraviolet–visible spectrophotometer equipped with a multicell thermoelectric temperature controller. The temperature was increased progressively at a ramp rate of 1 °C min^{-1}. The cloud point (T_c) values were determined as the maximum of the first-order derivatives of the curves, and the absorbance increase (ΔA) represents the difference between the maximum and the minimum absorbance values of the samples during the temperature ramp.

For the experiment to quantify the reversibility of condensation, a 20 µM protein with 100 mM NaCl sample was prepared on ice. It was then split into 4 Eppendorf tubes and a temperature ramp was carried out with the first one after centrifugation for 2 min at 5 °C and 15,000 r.p.m. Once the T_c and ΔA for condensation had been determined, the other 3 samples were heated 10 °C above the T_c for 2.5 min and then cooled to 10 °C below the T_c for 5 more min. This procedure was repeated 1, 2, or 3 times for each sample. Next, the samples were centrifuged for 2 min at 5 °C and 15,000 r.p.m., and a temperature ramp was carried out to determine their respective T_c and ΔA values (Extended Data Fig. 7d).

Microscopy in vitro

For microscopy imaging, 1.5 µl of sample was deposited in a sealed chamber comprising a slide and a coverslip sandwiching double-sided tape (3M 300 LSE high-temperature double-sided tape of 0.17 mm thickness). The coverslips used had been previously coated with PEG-silane following a published protocol[55]. The imaging was always performed on the surface of the coverslip, where the condensates had sedimented.

The DIC microscopy images were taken using an automated inverted Olympus IX81 microscope with a ×60/1.42 oil Plan APo N or a ×60/1.20 water UPlan SAPo objective using the Xcellence rt (v.1.2) software.

For fluorescence microscopy experiments, the purified proteins were labelled with DyLight 488 dye (DL488, Thermo Fisher Scientific) or Alexa Fluor 647 dye (AF647, Thermo Fisher Scientific). The labelling, as well as the calculation of the labelling percentage and the determination of the protein concentration, was performed following the provider's instructions. The final samples contained 0.5 µM of labelled protein and/or peptide out of the total indicated concentrations.

FRAP experiments were recorded using a Zeiss LSM780 confocal microscope system with a Plan ApoChromat ×63/1.4 oil objective. Condensates of similar size were selected, and the bleached region was 30% of their diameter. The intensity values were monitored for different ROIs: ROI 1 (bleached area), ROI 2 (entire condensate) and ROI 3 (background signal). The data were fitted using EasyFrap software[50] to extract the kinetic parameters of the experiment (recovery half-time and mobile fraction).

Super-resolution microscopy images of the multimers and their time evolution were taken at 25 °C in a Zeiss Elyra PS1 LSM 880 confocal microscope using the Fast Airyscan mode with an alpha Plan ApoChromat ×100/1.46 oil objective. The pixel size was kept constant at 40 nm.

Fluorescence microscopy images of the condensates and aggregates were taken at 37 °C in a Zeiss Elyra PS1 LSM 880 confocal microscope with an Airyscan detector using a Plan ApoChromat ×63/1.4 oil objective. The quantification of the aggregation process was done by image analysis using Fiji/ImageJ. The regions with the fluorescence signal not stemming from the background or the spherical condensates were selected. The percentage of the area of the field of view occupied by this selection corresponds to the aggregation value of the sample. The partitioning of the proteins in the condensates was calculated by image analysis using Fiji/ImageJ. The partitioning for each condensate was calculated by dividing the mean intensity of the condensate by the mean intensity of a ring of 1 µm thickness around the condensate.

RNA for in vitro experiments

The RNA used for in vitro experiments is a fragment of the 3′ UTR of cyclin B1 mRNA from *X. laevis* containing only one CPE site[56,57], 5′-AGUGUACAGUGUUUUUAAUAGUAUGUUG-3′. We used it as a control to study whether it influences the properties of the condensates. RNA caused a slight decrease in the phase-separation propensity of both isoforms, larger for nCPEB4(NTD) than for nCPEB4Δ4(NTD), which we attribute to interactions with positively charged amino acids involved in the intermolecular interactions driving condensation (Extended Data Fig. 5f). Notably, however, the presence of RNA in the samples did not alter their propensity to aggregate (Extended Data Fig. 5g).

Saturation concentration measurements

Saturation concentration measurements of nCPEB4(NTD) and the histidine to serine mutants were carried out by incubating the samples at 40 °C for 5 min, followed by centrifugation at 5,000 r.p.m. for 1.5 min at 40 °C. The concentration of protein in the supernatant (c_{sat}) was determined by absorbance measurement at 280 nm.

NMR spectroscopy

The samples were prepared as indicated in the section 'Sample preparation for in vitro experiments' using isotopically labelled protein (^{15}N- or ^{15}N,^{13}C-labelled). The prepared final samples were again pH adjusted to the desired value immediately before measurement. All the measurements were acquired at 5 °C using 3 mm NMR tubes with a sample volume of 200 µl.

All NMR experiments, except the diffusion measurements, were carried out on a Bruker Avance NEO 800 MHz spectrometer equipped with a TCI cryoprobe. All NMR samples contained 100 µM protein concentration (unless otherwise indicated) in 20 mM sodium phosphate buffer with 1 mM TCEP, 0.05% NaN_3, 7% D_2O and 2.5 µM DSS for referencing, at pH 8.0 (unless otherwise indicated). Samples with denaturant agent contained the indicated concentrations of d_4-urea.

A ^{15}N,^{13}C-labelled sample at 280 µM for nCPEB4(NTD) or 200 µM for nCPEB4Δ4(NTD) with 4 M urea at pH 7.0 was used for backbone resonance assignment. A series of nonlinear sampled 3D triple resonance experiments were recorded, including the BEST-TROSY version[58] of ^1H_N-detected HNCO, HN(CA)CO, HNCA, HN(CO)CA, HNCACB, HN(CO)

CACB and (H)N(CA)NH. Also, additional ^{1}Hα-detected HA(CA)CON and (HCA)CON(CA)H experiments[59] were measured for nCPEB4(NTD). Backbone resonance assignments were performed using CcpNmr[60] (v.2.4.2). The NMR assignments are available from the Biological Magnetic Resonance Data Bank (identifiers 51875 and 52346 for nCPEB4(NTD) and nCPEB4Δ4(NTD), respectively).

pH titrations from 7.0 to 8.0 were carried out to transfer NH assignments to the final experimental conditions. Standard 2D ^{1}H,^{15}N-HSQC or BEST-TROSY experiments were measured at 7.0 ≤ pH ≤ 7.25. 2D ^{1}H,^{15}N-CP-HISQC[61] experiments were used at pH ≥ 7.5 to reduce the effects of chemical exchange with water. For the urea titrations from 0 to 4 M at pH 8.0, ^{1}H,^{15}N-CP-HISQC experiments were measured. In the ^{1}H,^{15}N-CP-HISQC for the detection of arginine side-chain resonances, the ^{15}N carrier was placed at 85 ppm, and ^{13}C pulses for decoupling were centred at the chemical shift of $^{13}C_{\delta}$ (42 ppm) and $^{13}C_{\zeta}$ (158 ppm) arginine side chains.

Standard 2D ^{1}H,^{13}C-HSQC experiments of 500 μM ^{15}N,^{13}C-labelled nCPEB4(NTD) were measured in the absence and presence of 4 M urea to monitor specific amino acid side chains easily identifiable by their typical ^{1}H and ^{13}C random coil chemical shifts.

For histidine pK_a determination, 2D ^{1}H,^{13}C-HSQC spectra of 75 μM ^{15}N,^{13}C-labelled nCPEB4(NTD) were measured in the presence of 4 M urea at pH values between 5.58 and 8.31. The pH-induced changes of the chemical shifts of histidine side chains (^{1}H and ^{13}C, both aliphatic and aromatic) were fitted to a sigmoid function to obtain an apparent pK_a for all these histidine resonances in nCPEB4(NTD).

Non-uniform sampled experiments were processed using qMDD[62] (v.3.2). 2D ^{15}N-correlations (^{1}H,^{15}N-HSQC, ^{1}H,^{15}N-CP-HISQC, BEST-TROSY) and 2D ^{1}H,^{13}C-HSQC were processed using NMRPipe[63] and Topspin (v.4.0.8) (Bruker), respectively.

^{15}N-edited X-STE diffusion experiments[64] of 100 μM ^{15}N-labelled nCPEB4(NTD) in the absence and presence of 2 M urea were performed on a Bruker Avance III 600 MHz spectrometer equipped with a TCI cryoprobe. An encoding/decoding gradient length of 4.8 ms and a diffusion delay of 320 ms were used. The hydrodynamic diameter of nCPEB4(NTD) was estimated using dioxane as a reference molecule. Diffusion measurements under identical experimental conditions were carried out for dioxane, using in this case the PG-SLED sequence[65]. A gradient time (δ) of 1.6 ms and a diffusion time (Δ) of 70 ms were used. Diffusion coefficients were obtained by fitting the data to a mono-exponential equation using MestreNova (v.14.2.1-27684).

Dynamic light scattering

Dynamic light scattering (DLS) measurements were taken with a Zetasizer Nano-S instrument (Malvern) equipped with a He-Ne of 633 nm wavelength laser. Immediately before the measurement, the prepared samples were centrifuged for 5 min at 15,000 r.p.m. at 4 °C, and only the supernatant was subjected to measurement. Three measurements were performed for each sample, each of the measurements consisting of 10 runs of 10 s each. The experiments were carried out at 5 °C unless otherwise indicated. The deconvoluted hydrodynamic diameters arise from the mean of the peak of the intensity deconvolution of the data.

Size exclusion chromatography coupled to multi-angle light scattering

Size exclusion chromatography coupled to multiangle light scattering (SEC–MALS) experiments were performed by loading a 160 μM nCPEB4(NTD) with 0 mM NaCl sample into a Superose 6 increase 10/300 GL column (GE Healthcare) mounted on a Shimadzu Prominence Modular HPLC with a SPD-20 UV detector (Shimadzu) coupled to a Dawn Heleos-II multi-angle light scattering detector (18 angles, 658 nm laser beam) with an Optilab T-rEX refractometer (Wyatt Technology). The SEC-UV/MALS/RI system was equilibrated at 25 °C with 20 mM sodium phosphate buffer with 1 mM TCEP and 0.05% NaN_3 at pH 8.0. Data acquisition and processing were performed using Astra 6.1 software (Wyatt Technology).

Liquid-phase transmission electron microscopy

Transmission electron microscopy (TEM) experiments were performed on a 50 μM nCPEB4Δ4(NTD) sample with 0 mM NaCl. The sample was first imaged in solid-state TEM using the same set-up as described below for liquid-phase TEM (LPEM). Pre-screening samples in solid-state TEM before the LPEM imaging procedure is routinely done to pre-screen the structures that will be imaged in liquid later. The sample with no stain was deposited onto 400 mesh Cu grids, which were plasma discharged for 45 s to render them hydrophilic and to allow optimal sample wettability.

LPEM imaging was performed using a JEOL JEM-2200FS TEM microscope. The system was equipped with a field emission gun operating at 200 kV and an in-column Omega filter. The images were acquired with a direct detection device, the in-situ K2-IS camera (Gatan). The Ocean liquid holder, from DENSsolutions, was used to image the structure and dynamics of the specimens. The liquid samples were encased into two silicon nitride (Si_xN_y) chips. These chips had a 50-nm-thick Si_xN_y electron-transparent window of dimensions 10 × 200 μm. One of these chips had a 200 nm spacer that acts as a pillar and defines the liquid cell thickness, that is, *z* height, and hence the liquid thickness in the experiments. The chips were cleaned in HPLC-graded acetone followed by isopropanol for 5 min each to remove their protective layer made of poly(methyl methacrylate). Afterwards, the chips were plasma-cleaned for 13 min to increase their hydrophilicity. Next, 1.5 μl of non-stained sample was deposited on the previously prepared 200-nm-spacer chip. The drop-casted sample was enclosed by the spacer-less chip, thus sealing the liquid chamber. Then, 300 μl of the sample solution was flushed in the liquid holder at 20 μl min^{-1} with a syringe pump to ensure that the liquid cell inlet and outlet pipes were filled with the solution. We waited 5 min after collecting the sample solution from the outlet tube to minimize the convection effects from the flowing process. The liquid holder was introduced in the microscope, where imaging was performed in TEM mode and static conditions, that is, not in flow. To limit the electron beam dose (20 e^{-} $Å^{-2}$) on the specimen, images were collected at the minimum spot size (number 5) with a small condenser lens aperture (CLA number 3). For our investigations, dose fractionation videos were recorded in counted mode at 20 frames per s with the K2 camera. Every image was recorded in the format of 4-byte greyscale and required the full size of the detector.

The images and videos recorded were corrupted by noise, which significantly reduced the quality of the images, complicating any further analysis. Therefore, the Noise2Void (N2V) machine learning-based approach was adopted to overcome this problem[66]. Unlike the conventional machine learning-based approach, N2V reduces the noise of an image without any need for the corresponding noiseless image. This requirement makes the N2V ideal to process LPEM images, as noiseless images in liquid TEM are impossible to record. However, N2V requires an extensive dataset (also known as a training set) to fulfil its task, a common requirement to machine-learning-based approaches. Conventionally, the training set has to contain thousands of hundreds of images recorded with the same imaging settings to produce high-quality estimation of the noise distribution. Unfortunately, in our case, only single videos (image sequence) recorded at different imaging conditions were available. Therefore, the training set was created by sampling the image sequence every two frames to not bias the training process of the N2V. The remaining half of the image sequence was processed and used to derive the presented results.

To train the N2V, 3,050 frames were selected, extracting 128 different non-overlapping squared patches (that is, portions of the pixels of the image) of 64 × 64 pixels from each of them. Moreover, the N2V was iterated for 100 epochs, a trade-off value between performances and processing time. The training was performed by extracting 128

random patches (64 × 64 pixels) from each training image. These values produced the best results in a short processing time.

Molecular simulations

Molecular dynamics simulations were performed using the single-bead-per-residue model CALVADOS (v.2)[22,23] implemented in OpenMM (v.7.5)[67]. All simulations were conducted in the NVT ensemble at 20 °C using a Langevin integrator with a time step of 10 fs and friction coefficient of 0.01 ps^{-1}. In our simulations, pH was modelled through its effect on the charge of the histidine residues (q_{His})[68].

Direct coexistence simulations were performed with 100 chains in a cuboidal box of side lengths $[L_x, L_y, L_z] = [25, 25, 300]$ nm. Simulations were run in $n = 3$ independent replicas for at least 55 µs each. The systems readily formed a protein-rich slab spanning the periodic boundaries along the x and y coordinates. The initial 2 µs of the simulation trajectories were discarded, and time-averaged concentration profiles along the z axis were calculated after centring the condensates in the box as previously described[22].

To model protein multimers, 400 chains were initially placed at random positions in a cubic box of side length 188 nm and simulations were run in $n = 2$ replicas for 16 µs each. The formation and dissolution of protein multimers was monitored using a cluster analysis implemented in OVITO[69]. Proteins were clustered on the basis of the distances between their centres of mass, using a cut-off of 1.5 times the average radius of gyration of the protein. Contact maps were calculated between a chain in the middle of the condensate or multimer and the surrounding chains. Contacts were quantified using the switching function $c(r) = 0.5 - 0.5 \times \tanh[(r - \sigma_0)/r_0]$, where r is the intermolecular distance between two residues, $\sigma_0 = 1$ nm, and $r_0 = 0.3$ nm.

To match the conditions of the experiments with which the simulation results are compared, direct coexistence and multimer simulations were performed at ionic strengths of 150 mM and 60 mM, respectively. Configurations were saved every 2 ns for slabs and every 5 ns for multimer simulations.

Simulation trajectories were analysed using MDTraj[70] (v.1.9.6) and MDAnalysis[71,72] (v.1.1). The molecular visualizations presented in Fig. 2j were generated using VMD[73] (v.1.9.4).

Characterization of the multimers

To investigate which specific residues of nCPEB4(NTD) drive its condensation, we used solution NMR spectroscopy, a technique that can provide residue-specific information on the conformation and interactions of intrinsically disordered proteins[74]. Indeed, when conditions are insufficient for condensation, the same interactions driving this process can cause the monomer to collapse into a state that can be characterized at residue resolution, thus providing this key information[75]. Under such conditions (Supplementary Fig. 5a), nCPEB4(NTD) had a spectrum characteristic of a collapsed intrinsically disordered protein, in which only 13% of the NMR signals were visible (Supplementary Fig. 5b, in light green). We analysed the sample by DLS to confirm its monomeric nature, but we detected only nCPEB4(NTD) multimers with a hydrodynamic diameter of approximately 55 nm, which is much larger than that predicted for a monomer[76] (approximately 11 nm) (Supplementary Fig. 5c).

To characterize the multimers, also known as clusters, which have also been observed for phase-separating proteins with intrinsically disordered domains[77–80], we first determined whether their formation is reversible. To this end, we performed DLS analysis of increasingly diluted samples of nCPEB4(NTD) under the same solution conditions. We observed that at 0.5 µM, the multimers seemed to be in equilibrium with a species with a hydrodynamic diameter close to that predicted for the monomer (Extended Data Fig. 3e, in green). Next, at this concentration, we modified solution conditions to favour condensation by increasing the temperature and ionic strength, as well as by decreasing the pH. In all cases, we observed a decrease in the signal corresponding to the monomer and an increase in that corresponding to multimers, thus indicating a shift of the multimerization equilibrium (Extended Data Fig. 3e). This result suggests that the nCPEB4(NTD) multimers are stabilized by the same types of interactions as the condensates (Extended Data Fig. 1m and Fig. 2e,k).

These findings prompted us to study whether these multimers grow over time to become condensates observable by optical and fluorescence microscopy, that is, whether they represent intermediates in the condensation pathway. To this end, we first analysed, over 15 h, samples of freshly prepared nCPEB4(NTD) multimers by DLS. We observed a progressive increase in size and polydispersity up to an average hydrodynamic diameter of approximately 90 nm and a polydispersity index of approximately 0.10 (Supplementary Fig. 5d). We also determined the morphology of the multimers at the nanoscale by LPEM, confirming that they are spherical and have a diameter of 30–50 nm (Extended Data Fig. 3f and Supplementary Fig. 5e). Finally, super-resolution microscopy confirmed that the multimers grow with time, thus becoming larger spherical particles resembling condensates (Extended Data Fig. 3g). It is possible that the nCPEB4 multimers here identified correspond to mesoscopic condensates, equivalent to those observed by optical microscopy, albeit smaller; however, as their dimensions preclude their thorough physical characterization, we consider it appropriate to consider them distinct species in this work.

We next carried out experiments to determine the nature of the species giving rise to the residue-specific NMR signals observed in the presence of multimers. To this end, we analysed a sample of multimers by SEC–MALS. This approach showed that the multimers are assemblies of approximately 350 nCPEB4(NTD) molecules (Supplementary Fig. 5f), corresponding to a molecular weight of approximately 1.7×10^7 Da. Next, we performed ^{15}N-edited X-STE experiments to measure the diffusion coefficient of the species giving rise to the signals detected by NMR, from which we derived that they diffuse much more slowly than a monomer, with a value in semi-quantitative agreement with that obtained by DLS and LPEM (Supplementary Fig. 5g), thereby indicating that they correspond mainly to multimers. We concluded that solution NMR can be used to identify the most flexible regions of the nCPEB4(NTD) sequence under conditions in which it forms multimers, presumably corresponding to those least involved in the interactions stabilizing them[81–83].

To assign the NMR signals to specific residues, we progressively added urea and observed that at 1.5–2 M, the urea concentration necessary to dissociate the multimers, the signals of most residues could be detected (Extended Data Fig. 3h,i and Supplementary Fig. 5b) and stemmed from a species with the diffusion coefficient expected for a nCPEB4(NTD) monomer (Supplementary Fig. 5g). A comparison of the spectra obtained in the absence and presence of denaturant revealed that the signals observed for the multimer corresponded to residues between positions approximately 50 and 150 in the sequence of nCPEB4(NTD): this region of sequence is devoid of aromatic and positively charged residues and instead rich in negatively charged ones (Extended Data Fig. 3h,j). Despite the presence of 4 M urea, the spectrum of monomeric nCPEB4(NTD) had a wide range of intensities. An analysis of signal intensity as a function of residue type revealed particularly low values for histidine and arginine (Extended Data Fig. 3k), which suggested that these residue types are involved in transient interactions and explain the very low signal intensity of the histidine-rich HClust (residues 229–252) and the arginine-rich me4 (residues 403–410) (Extended Data Fig. 3h).

To facilitate the interpretation of these results, we monitored the formation of nCPEB4(NTD) multimers in molecular simulations performed using the CALVADOS model[22,23]. Contacts calculated between a chain in the centre of the multimer and the surrounding chains in assemblies of 130–170 chains showed that the C-terminal region, including HClust and me4, is more involved in intermolecular interactions than the N-terminal region rich in aspartate and glutamate residues (positions

72–147) (Extended Data Fig. 3l). The simulations therefore support the conclusion that the decreased NMR signal intensity in the C-terminal region reflects an increased number of contacts of these residues within the condensates. Finally, to further characterize the interactions stabilizing the multimers, we performed ^{1}H,^{13}C-HSQC experiments to analyse the intensity of side-chain signals without urea, when nCPEB4(NTD) is multimeric, and in 4 M urea, when nCPEB4(NTD) is instead monomeric (Extended Data Fig. 3m and Supplementary Fig. 5h–j). We observed that the intensities, especially those of the signals corresponding to histidine, tryptophan and arginine residues, are lower for the former than for the latter. We also performed ^{1}H,^{15}N-CP-HISQC experiments to study the arginine side-chain NH signals in the same samples and found that they are undetectable in the absence of the denaturant but can be observed in its presence (Supplementary Fig. 5k). Taken together, our results indicate that the multimers formed by nCPEB4(NTD) on the condensation pathway are stabilized mainly by interactions involving histidine and arginine residues, which are predominantly located in the C-terminal region (Supplementary Fig. 5l).

Protein sequence analysis

Cprofiler (http://www.cprofiler.org/) was used to determine the enrichment score of each amino acid type in the protein sequence compared with the DisProt3.4 database[84,85]. The protein sequences analysed correspond to residues 1–448 for nCPEB4(NTD) (UniProt identifier Q17RY0-2), residues 1–311 for CPEB2(NTD) (UniProt identifier Q7Z5Q1-3) and residues 1–452 for CPEB3(NTD) (UniProt identifier Q7TN99-1).

Reporting summary

Further information on research design is available in the Nature Portfolio Reporting Summary linked to this article.

Data availability

The NMR assignments are available from the Biological Magnetic Resonance Data Bank (identifiers 51875 and 52346). The simulation data generated in this study are available at GitHub (https://github.com/KULL-Centre/_2023_Garcia-Cabau_CPEB4). Protein sequences correspond to UniProt identifiers Q17RY0 for CPEB4, Q7Z5Q1 for CPEB2 and Q7TN99 for CPEB3. Source data are provided with this paper.

Code availability

The simulations were performed using CALVADOS (v.2) available at GitHub (https://github.com/KULL-Centre/CALVADOS). The code for repeating the simulation analyses is available at GitHub (https://github.com/KULL-Centre/_2023_Garcia-Cabau_CPEB4) and at Zenodo (https://doi.org/10.5281/zenodo.13880099)[86].

45. Calderone, V. et al. Sequential functions of CPEB1 and CPEB4 regulate pathologic expression of vascular endothelial growth factor and angiogenesis in chronic liver disease. *Gastroenterology* **150**, 982–97.e30 (2016).
46. Halfmann, R. & Lindquist, S. Screening for amyloid aggregation by semi-denaturing detergent–agarose gel electrophoresis. *J. Vis. Exp.* **17**, 838 (2008).
47. Berrow, N. S. et al. A versatile ligation-independent cloning method suitable for high-throughput expression screening applications. *Nucleic Acids Res.* **35**, e45 (2007).
48. Belloc, E. & Méndez, R. A deadenylation negative feedback mechanism governs meiotic metaphase arrest. *Nature* **452**, 1017–1021 (2008).
49. Raj, B. et al. A global regulatory mechanism for activating an exon network required for neurogenesis. *Mol. Cell* **56**, 90–103 (2014).
50. Rapsomaniki, M. A. et al. easyFRAP: an interactive, easy-to-use tool for qualitative and quantitative analysis of FRAP data. *Bioinformatics* **28**, 1800–1801 (2012).
51. Chávez, J. C., Darszon, A., Treviño, C. L. & Nishigaki, T. Quantitative intracellular pH determinations in single live mammalian spermatozoa using the ratiometric dye SNARF-5F. *Front. Cell Dev. Biol.* **7**, 366 (2019).
52. de Moor, C. H. & Richter, J. D. Cytoplasmic polyadenylation elements mediate masking and unmasking of cyclin B1 mRNA. *EMBO J.* **18**, 2294–2303 (1999).
53. Marley, J., Lu, M. & Bracken, C. A method for efficient isotopic labeling of recombinant proteins. *J. Biomol. NMR* **20**, 71–75 (2001).
54. Escobedo, A., Chiesa, G. & Salvatella, X. in *Intrinsically Disordered Proteins: Methods and Protocols* (eds Kragelund, B. B. & Skriver, K.) 211–231 (Springer US, 2020).
55. Alberti, S. et al. A user's guide for phase separation assays with purified proteins. *J. Mol. Biol.* **430**, 4806–4820 (2018).
56. Piqué, M., López, J. M., Foissac, S., Guigó, R. & Méndez, R. A combinatorial code for CPE-mediated translational control. *Cell* **132**, 434–448 (2008).
57. Weill, L., Belloc, E., Castellazzi, C. L. & Méndez, R. Musashi 1 regulates the timing and extent of meiotic mRNA translational activation by promoting the use of specific CPEs. *Nat. Struct. Mol. Biol.* **24**, 672–681 (2017).
58. Solyom, Z. et al. BEST-TROSY experiments for time-efficient sequential resonance assignment of large disordered proteins. *J. Biomol. NMR* **55**, 311–321 (2013).
59. Mäntylahti, S., Hellman, M. & Permi, P. Extension of the HA-detection based approach: (HCA)CON(CA)H and (HCA)NCO(CA)H experiments for the main-chain assignment of intrinsically disordered proteins. *J. Biomol. NMR* **49**, 99–109 (2011).
60. Vranken, W. F. et al. The CCPN data model for NMR spectroscopy: development of a software pipeline. *Proteins* **59**, 687–696 (2005).
61. Yuwen, T. & Skrynnikov, N. R. CP-HISQC: a better version of HSQC experiment for intrinsically disordered proteins under physiological conditions. *J. Biomol. NMR* **58**, 175–192 (2014).
62. Mayzel, M., Rosenlöw, J., Isaksson, L. & Orekhov, V. Y. Time-resolved multidimensional NMR with non-uniform sampling. *J. Biomol. NMR* **58**, 129–139 (2014).
63. Delaglio, F. et al. NMRPipe: a multidimensional spectral processing system based on UNIX pipes. *J. Biomol. NMR* **6**, 277–293 (1995).
64. Ferrage, F., Zoonens, M., Warschawski, D. E., Popot, J.-L. & Bodenhausen, G. Slow diffusion of macromolecular assemblies by a new pulsed field gradient NMR method. *J. Am. Chem. Soc.* **125**, 2541–2545 (2003).
65. Wilkins, D. K. et al. Hydrodynamic radii of native and denatured proteins measured by pulse field gradient NMR techniques. *Biochemistry* **38**, 16424–16431 (1999).
66. Krull, A., Buchholz, T.-O. & Jug, F. Noise2Void—learning denoising from single noisy images. Preprint at https://doi.org/10.48550/arXiv.1811.10980 (2018).
67. Eastman, P. et al. OpenMM 7: rapid development of high performance algorithms for molecular dynamics. *PLoS Comput. Biol.* **13**, e1005659 (2017).
68. Nagai, H., Kuwabara, K. & Carta, G. Temperature dependence of the dissociation constants of several amino acids. *J. Chem. Eng. Data* **53**, 619–627 (2008).
69. Stukowski, A. Visualization and analysis of atomistic simulation data with OVITO—the open visualization tool. *Modell. Simul. Mater. Sci. Eng.* **18**, 015012 (2009).
70. McGibbon, R. T. et al. MDTraj: a modern open library for the analysis of molecular dynamics trajectories. *Biophys. J.* **109**, 1528–1532 (2015).
71. Michaud-Agrawal, N., Denning, E. J., Woolf, T. B. & Beckstein, O. MDAnalysis: a toolkit for the analysis of molecular dynamics simulations. *J. Comput. Chem.* **32**, 2319–2327 (2011).
72. Gowers, R. J. et al. MDAnalysis: a Python package for the rapid analysis of molecular dynamics simulations. *SciPy Proc.* https://doi.org/10.25080/Majora-629e541a-00e (2016).
73. Humphrey, W., Dalke, A. & Schulten, K. VMD: visual molecular dynamics. *J. Mol. Graph.* **14**, 33–38 (1996).
74. Dyson, H. J. & Wright, P. E. Unfolded proteins and protein folding studied by NMR. *Chem. Rev.* **104**, 3607–3622 (2004).
75. Bremer, A. et al. Deciphering how naturally occurring sequence features impact the phase behaviours of disordered prion-like domains. *Nat. Chem.* **14**, 196–207 (2022).
76. Marsh, J. A. & Forman-Kay, J. D. Sequence determinants of compaction in intrinsically disordered proteins. *Biophys. J.* **98**, 2383–2390 (2010).
77. Martin, E. W. et al. A multi-step nucleation process determines the kinetics of prion-like domain phase separation. *Nat. Commun.* **12**, 4513 (2021).
78. Kar, M. et al. Phase-separating RNA-binding proteins form heterogeneous distributions of clusters in subsaturated solutions. *Proc. Natl Acad. Sci. USA* **119**, e2202222119 (2022).
79. Ray, S. et al. Mass photometric detection and quantification of nanoscale α-synuclein phase separation. *Nat. Chem.* **15**, 1306–1316 (2023).
80. Gil-Garcia, M. et al. Local environment in biomolecular condensates modulates enzymatic activity across length scales. *Nat. Commun.* **15**, 3322 (2024).
81. Christodoulou, J. et al. Heteronuclear NMR investigations of dynamic regions of intact *Escherichia coli* ribosomes. *Proc. Natl Acad. Sci. USA* **101**, 10949–10954 (2004).
82. Baldwin, A. J. et al. Cytochrome display on amyloid fibrils. *J. Am. Chem. Soc.* **128**, 2162–2163 (2006).
83. Klein-Seetharaman, J. et al. Long-range interactions within a nonnative protein. *Science* **295**, 1719–1722 (2002).
84. Sickmeier, M. et al. DisProt: the Database of Disordered Proteins. *Nucleic Acids Res.* **35**, D786–D793 (2007).
85. Vacic, V., Uversky, V. N., Dunker, A. K. & Lonardi, S. Composition Profiler: a tool for discovery and visualization of amino acid composition differences. *BMC Bioinformatics* **8**, 211 (2007).
86. Tesei, G. & Lindorff-Larsen, K. Molecular simulations of the N-terminal domain of CPEB4. *Zenodo* https://doi.org/10.5281/zenodo.13880099 (2024).

Acknowledgements We thank B. Bolognesi, I. Fariñas, E. Giralt, J. Guillén-Boixet, D. Hnisz, M. Irimia, G. Montoya and M. Palacín for suggestions; staff at the Biostatistics/Bioinformatics, Advanced Digital Microscopy and Mass Spectrometry and Proteomics Facilities at IRB Barcelona and the Spanish ICTS Red de Laboratorios de RMN de biomoléculas (R-LRB) for their support; A. García de Herreros and A. Zorzano for providing NmumG and C2C12 cell lines, respectively; and I. Latorre and J.M. Valverde for help with protein expression and purification. C.G.-C. acknowledges a graduate fellowship from MINECO (PRE2018-084684). A. Bartomeu acknowledges a graduate fellowship from MINECO (PRE2018-083790). K.C.C. acknowledges a Hong Kong PhD fellowship from the Hong Kong Research Grants Council (PF21-62132). L.R.-P. is a Serra Húnter Fellow. R.H. was supported by the Enhanced New Staff Start-up Research Grant (The University of Hong Kong). J.P.-U. acknowledges a Juan de la Cierva fellowship from MCIN/AEI (FJC2021-046999-I). J.J.L. acknowledges grants from the Spanish Ministry of Science and Innovation (MCIN/AEI/FEDER,UE; PID2021-123141OB-I00) and CIBER-NED. CBMSO is a Severo Ochoa Center of Excellence (MICIN, award CEX2021-001154-S). K.L.-L. acknowledges support from the Novo Nordisk Foundation (PRISM; NNF18OC0033950). K.L.-L. acknowledges

access to computational resources from the Danish National Supercomputer for Life Sciences (Computerome). This project has also received funding from the European Union's Horizon 2020 research and innovation programme under the Marie Skodowska-Curie grant agreement number 101025063. R.M. was supported by grants from the Spanish Ministry of Science, Innovation and Universities (PID2020-119533GB-I00 and PDC2021-121716-I00), and the Spanish Association Against Cancer (AECC) (GCB15152955MÉND), the Worldwide Cancer Research Foundation (20-0284), World Cancer Research Fund International (2020_021), the BBVA Foundation (BBVABIOMED/18), La Caixa Foundation (LCF/PR/HR19/52160020), and the Fundacio Marato TV3 (201926-30-31). X.S. was supported by AGAUR (2017 SGR 324), MINECO (BIO2015-70092-R and PID2019-110198RB-I00), and the European Research Council (CONCERT, contract number 648201). CBMSO and IRB Barcelona are the recipients of a Severo Ochoa Award of Excellence from MINECO (Government of Spain).

Author contributions Conceptualization: C.G.-C., A. Bartomeu, R.M. and X.S. Methodology: C.G.-C., A. Bartomeu, A. Balaceanu, G.T., K.C.C., B.D.-A., M.F.-A., J.M. and C.D.P. Investigation and formal analyses: C.G.-C., A. Bartomeu, A. Balaceanu, G.T., K.C.C., J.P.-U., S.P., B.D.-A., M.F.-A., C.D.P. and L.R.-P. Supervision: J.G., L.R.-P., G.B., R.H., J.J.L., K.L.-L., R.M. and X.S. Writing of original draft: C.G.-C., A. Bartomeu, R.M. and X.S. Writing, reviewing and editing: all authors. Funding acquisition: G.B., R.H., J.J.L., K.L.-L., R.M. and X.S.

Competing interests K.L.-L. holds stock options in and is a consultant for Peptone. X.S. is a scientific founder and advisor of Nuage Therapeutics. All other authors declare no competing interests.

Additional information

Supplementary information The online version contains supplementary material available at https://doi.org/10.1038/s41586-024-08289-w.

Correspondence and requests for materials should be addressed to Raúl Méndez or Xavier Salvatella.

Peer review information *Nature* thanks the anonymous reviewers for their contribution to the peer review of this work. Peer reviewer reports are available.

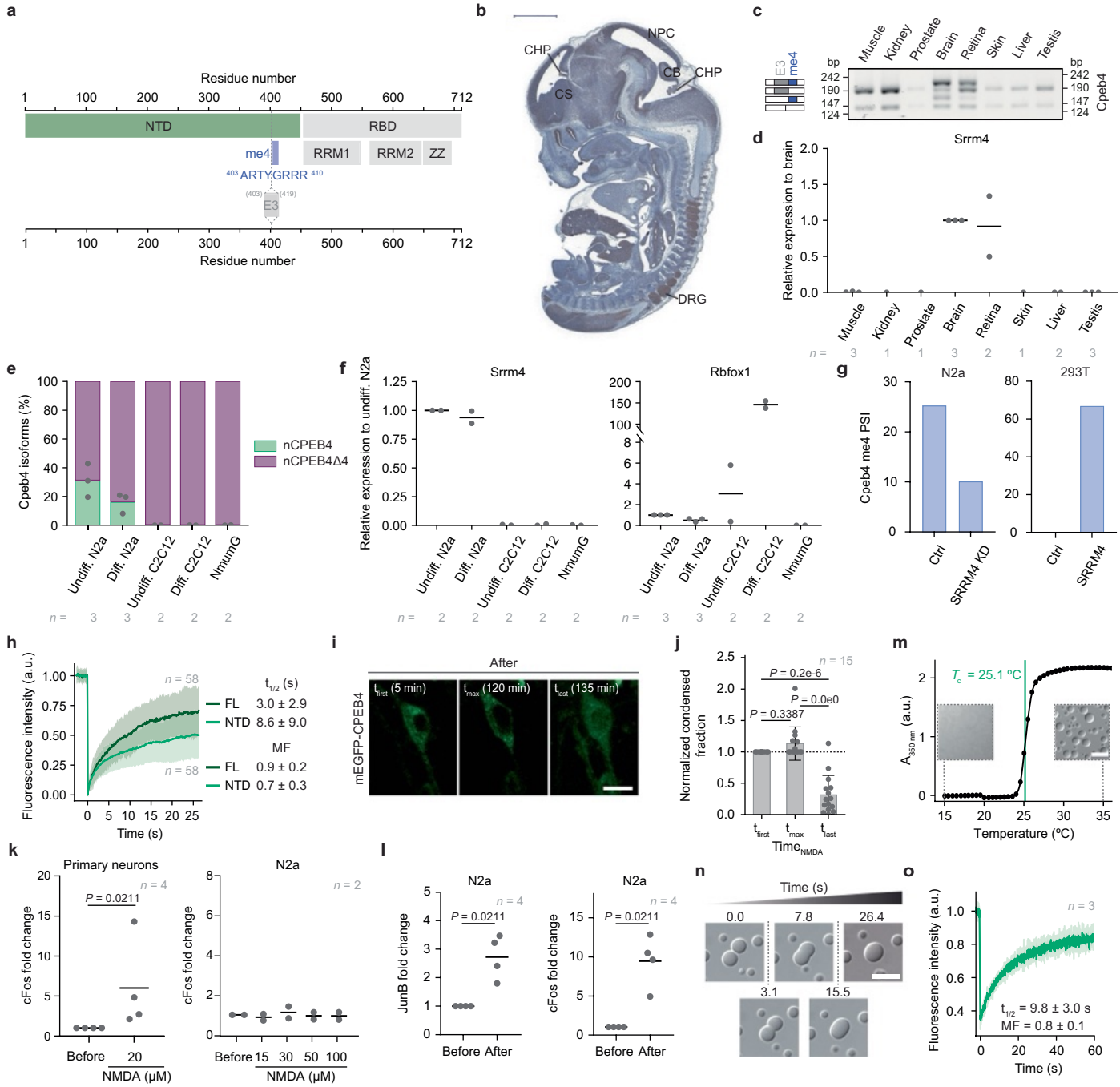

Extended Data Fig. 1 | See next page for caption.

Extended Data Fig. 1 | Model systems and in vitro behavior. a) nCPEB4 sequence. E3, exon 3; me4, microexon 4; RRM, RNA recognition motif; ZZ, zinc-binding domain. **b)** Sagittal section of a CPEB4 immunohistochemistry in a mouse embryo (E13.5) with several regions of the nervous system highlighted. CB, cerebellum; CHP, choroid plexus; CS, corpus striatum; DRG, dorsal root ganglion; NPC, neopallial cortex. Representative of $n = 3$ embryos. **c)** RT-PCR assay monitoring Cpeb4 me4 splicing in different mouse organs with an amplified schematic of the Cpeb4 splice variants. $n = 2$ replicates. **d)** qRT-PCR assays monitoring Srrm4 transcript levels in different mouse organs relative to brain (mean). *n*, biological replicates (tissue samples from different mice). **e)** qRT-PCR assays monitoring the percentage of Cpeb4 isoforms harboring me4 (nCPEB4) or not (nCPEB4Δ4) in different cell lines (mean). Undiff., undifferentiated; Diff., differentiated. *n*, biological replicates. **f)** qRT-PCR assays monitoring Srrm4 and Rbfox1 transcript levels in different cell lines relative to undifferentiated N2a (mean). *n*, biological replicates. **g)** Percentage spliced in (PSI) of Cpeb4 me4 in either Control (Ctrl) or SRRM4 knock-down (SRRM4 KD) N2a cells and in either Control (Ctrl) or SRRM4 over-expressed (SRRM4) 293T cells. Data from B. Blencowe[49]. **h)** FRAP of nCPEB4 in N2a cells (mean ± s.d.). Fluorescence recovery half-time ($t_{1/2}$) and mobile fraction (MF) from 3 independent experiments. *n*, foci. **i,j)** Fluorescence microscopy of live ex vivo striatal neurons after stimulation with NMDA (*i*) and fraction of the cellular area occupied by condensates after stimulation, normalized to the value measured at the end of stimulation, t_{first} (*j*) (mean ± s.d., one-way ANOVA). t_{first}, time frame immediately after NMDA addition; t_{max}, time frame showing the maximum condensed fraction; t_{last}, last time frame. *n*, cells. **k)** Fold change in the transcript levels (mean, two-tailed Mann-Whitney test) of the early depolarization marker cFos in NMDA stimulated primary neurons and N2a cells relative to before stimulation. *n*, independent experiments. **l)** Fold change in the transcript levels (mean, two-tailed Mann-Whitney test) of early depolarization markers (JunB and cFos) in N2a cells after KCl stimulation relative to before stimulation. *n*, independent experiments. **m)** Absorbance as a function of temperature of a nCPEB4(NTD) solution (30 μM protein, 100 mM NaCl) and DIC microscopy insets at 15 and 35 °C. Green line: cloud point (T_c). Representative of $n = 3$ independent measurements. **n)** DIC microscopy of a fusion event of nCPEB4(NTD) in vitro condensates (30 μM protein, 100 mM NaCl, 25 °C). $n = 2$ fusion events. **o)** FRAP of nCPEB4(NTD) in vitro condensates (20 μM protein, 150 mM NaCl, 37 °C; mean ± s.d.). *n*, condensates. For *j*, only cells showing cytoplasmic foci before stimulation were analyzed. For gel source data, see Supplementary Fig. 1. Scale bars, 1000 μm (*b*) and 10 μm (*i,m,n*).

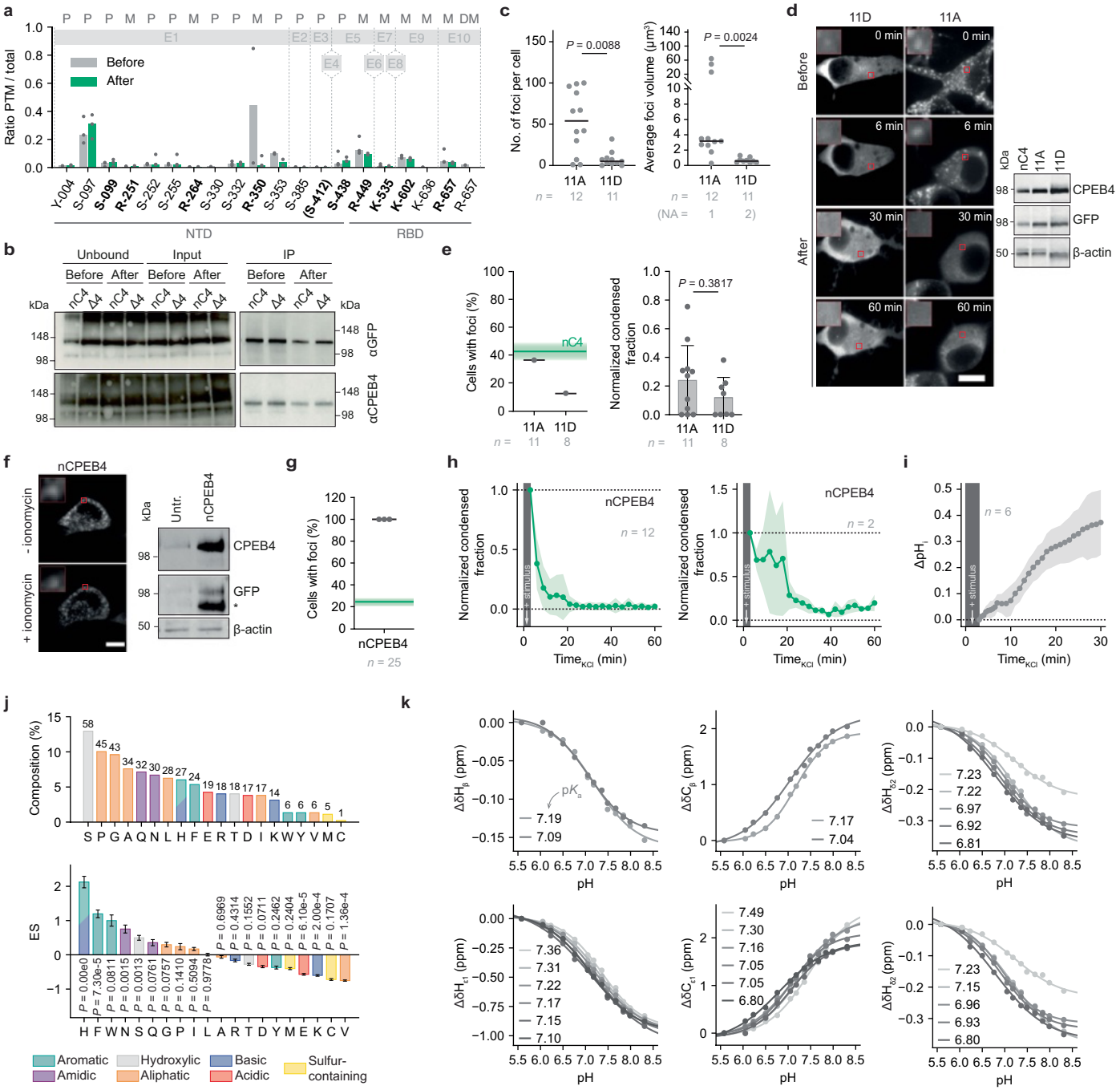

Extended Data Fig. 2 | See next page for caption.

Extended Data Fig. 2 | Analysis of phosphorylations and pH titrations. **a,b)** nCPEB4 modified-to-total occurrence ratios determined by mass spectrometry (*a*) before and after stimulation of N2a cells overexpressing FL nCPEB4-GFP (median) and representative WB of the immunoprecipitation (*b*). $n = 3$ independent biological replicates. Bold: previously undescribed post-translationally modified sites. Gray line: positions of exons (E1-E10). E4, microexon 4; P, phosphorylation; M, methylation; DM, dimethylation. **c)** Foci quantification of nCPEB4(NTD)-GFP non-phosphorylatable (11A) and phospho-mimetic (11D) mutants in differentiated N2a cells (median, two-tailed Mann-Whitney test). *n*, cells. **d)** Fluorescence microscopy of live differentiated N2a cells overexpressing nCPEB4(NTD)-GFP 11D and 11A mutants before and after stimulation with WB analyzing expression. $n_{11D} = 8$ and $n_{11A} = 11$ cells from 1 independent experiment. **e)** Left: Percentage of cells (mean) in *d*) with foci after stimulation (60 min). The mean ± s.d. of nCPEB4(NTD) is represented in green for reference (Fig. 1j). Right: Fraction of cellular area in *d*) occupied by condensates after stimulation (60 min), normalized to the value measured at the end of stimulation (mean ± s.d., two-tailed Mann-Whitney test). *n*, cells from 1 independent experiment. **f,g)** Fluorescence microscopy of live differentiated N2a cells overexpressing nCPEB4-GFP before (-ionomycin) and after (+ionomycin) addition of 1 µM ionomycin with WB analyzing expression (*f*) and percentage of cells (mean) with foci after ionomycin addition (60 min) (g). The mean ± s.d. of KCl stimulation is represented in green for reference (Fig. 1j). Untr., untransfected cells. *n*, cells from 3 independent experiments. **h)** Fraction of cellular area occupied by condensates after stimulation, normalized to the value measured at the end of stimulation. Representation of the behavior of 40% (left) and 6.7% (right) of cells (mean ± s.d.). *n*, cells out of 30 total cells. Related to Fig. 2b. **i)** Changes in intracellular pH of N2a cells after stimulation. Representation of the behavior of 46.2% of cells (mean ± s.d.). *n*, cells out of 13 total cells from 3 independent experiments. Related to Fig. 2c. **j)** Amino acid composition of nCPEB4(NTD) and enrichment score (ES, mean ± s.d.) of each amino acid type in nCPEB4(NTD) compared to the DisProt3.4 database[84,85]. **k)** Determination of the apparent pK_a of His residues in nCPEB4(NTD) by NMR, where each plot represents the fit of the chemical shift of the His resonances and the inset shows the pK_a values obtained. For *e*,*g*,*h*, only cells with cytoplasmic foci before stimulation were analyzed. nC4, nCPEB4; Δ4, nCPEB4Δ4. For gel source data, see Supplementary Fig. 2. Scale bars, 10 µm (*d*,*f*).

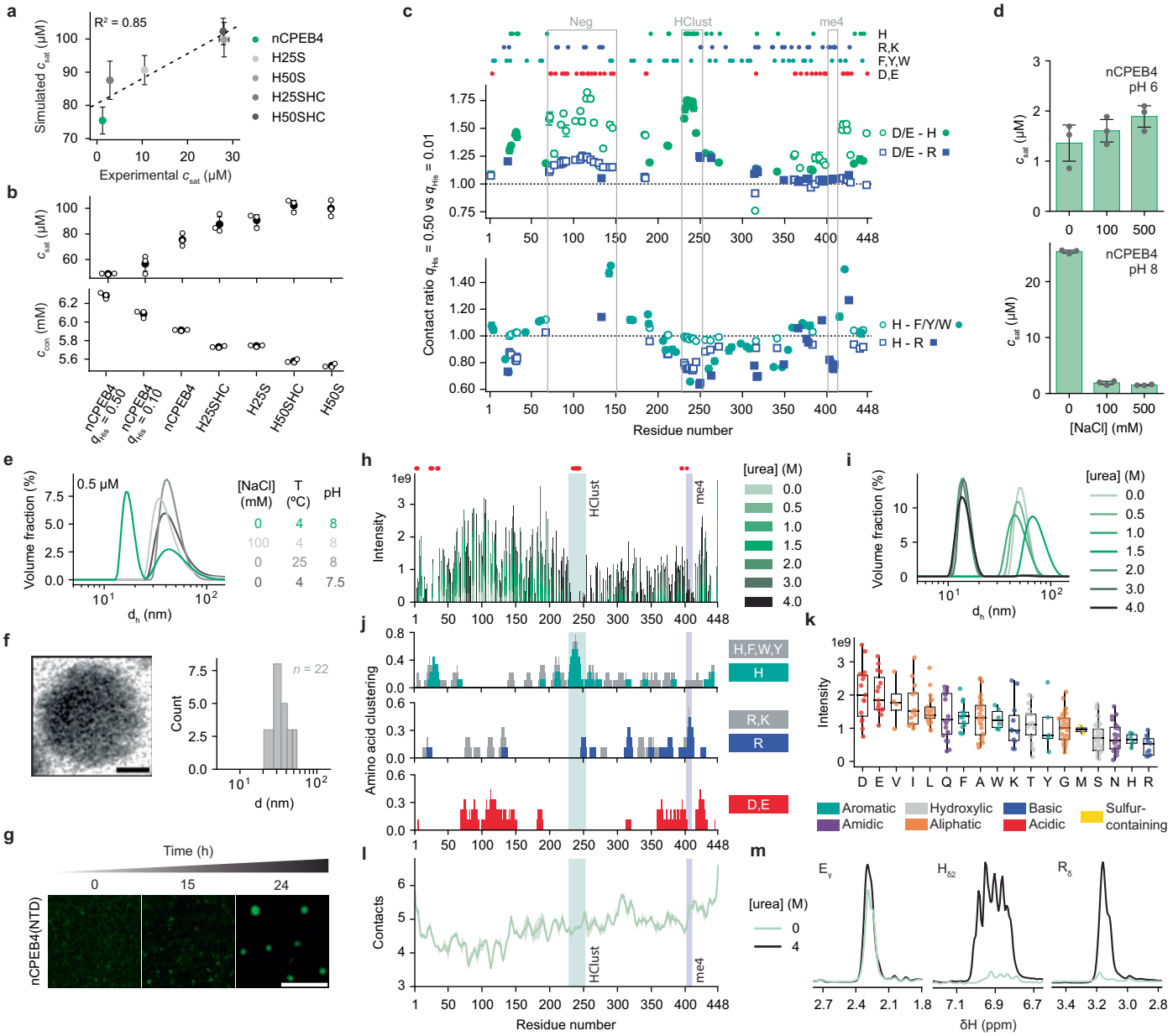

Extended Data Fig. 3 | See next page for caption.

Extended Data Fig. 3 | nCPEB4(NTD) simulations and analysis of multimerization. a) Comparison between the saturation concentrations from experiments (30 μM protein, 100 mM NaCl, pH 8, 40 °C) and molecular simulations (q_{His} = 0.01, 20 °C) of nCPEB4(NTD) and the His to Ser variants. Experimental saturation concentrations are represented as mean ± s.d. of n = 3 measurements of the same sample. Simulation data are represented as mean ± s.d. over n = 3 independent simulation replicas. q_{His}, charge of His residues. **b)** Saturation concentrations (upper) and dense phase concentrations (lower) from molecular simulations of nCPEB4(NTD) with q_{His} = 0.50 (nCPEB4 q_{His} = 0.50), 0.10 (nCPEB4 q_{His} = 0.10), and 0.01 (nCPEB4), and of the His to Ser variants with q_{His} = 0.01. Data represented as mean ± s.d. (closed markers) over n = 3 independent simulation replicas (open markers). **c)** Upper: position of His, Arg, Lys, Phe, Tyr, Trp, Asp, and Glu residues in the nCPEB4(NTD) sequence. Middle: ratio of contacts at q_{His} = 0.50 vs q_{His} = 0.01 between His (green circles) or Arg residues (blue squares) and charged residues (closed symbols), and vice versa (open circles). Lower: ratio of contacts at q_{His} = 0.50 vs q_{His} = 0.01 between aromatic (cyan circles) or Arg residues (blue squares) and His residues (closed symbols), and vice versa (open symbols). Both open and closed symbols show ratios of contacts between residues on a chain in the middle of the condensate and the surrounding chains. Data represented as mean ± s.d. of n = 3 independent simulation replicas. **d)** Experimental saturation concentrations (30 μM protein, 40 °C) of nCPEB4(NTD) at increasing NaCl concentrations at pH 6 and 8 (mean ± s.d.). n = 3 measurements of the same sample. **e)** Effect of concentration, temperature, ionic strength, and pH on nCPEB4(NTD) multimer formation monitored by DLS (representative of n = 3 measurements). **f)** Liquid-phase TEM micrograph of a multimer and size distribution. n, imaged multimers. Scale bar, 10 nm. **g)** Temporal evolution of multimers (10 μM protein, 100 mM NaCl, 25 °C) by super-resolution microscopy. n = 2 fields of view. Scale bar, 5 μm. **h)** ^{1}H,^{15}N-CP-HISQC backbone amide peak intensities of nCPEB4(NTD) at increasing urea concentrations (100 μM protein, 5 °C). Red dots: residues not assigned. n = 1 spectrum. **i)** Urea titration of the samples in *h)* monitored by DLS (representative of n = 3 measurements). **j)** Amino acid clustering (nine amino acid window) in nCPEB4(NTD). Upper: aromatic residues (gray) and His (cyan). Center: cationic residues (gray) and Arg (blue). Lower: anionic residues (red). **k)** Ranking of mean ^{1}H,^{15}N-CP-HISQC backbone amide peak intensities of nCPEB4(NTD) at 4 M urea by amino acid type (100 μM protein, 5 °C). Box plots: line, median; box, quartiles; whiskers, 1.5x interquartile range. n = 1 spectrum. **l)** Average contacts (mean and difference of n = 2 independent replicas) between residues in a chain in the middle of a multimer and the residues on the surrounding chains from simulations of nCPEB4(NTD) multimers of 130 to 170 chains with an Rg of 17.5 ± 0.8 nm. **m)** ^{1}H,^{13}C-HSQC traces of representative side chain resonances at 0 and 4 M urea (500 μM protein, 5 °C). The specific residue types (one letter code) and ^{1}H position within the side chain (Greek letters) are indicated. n = 1 spectrum.

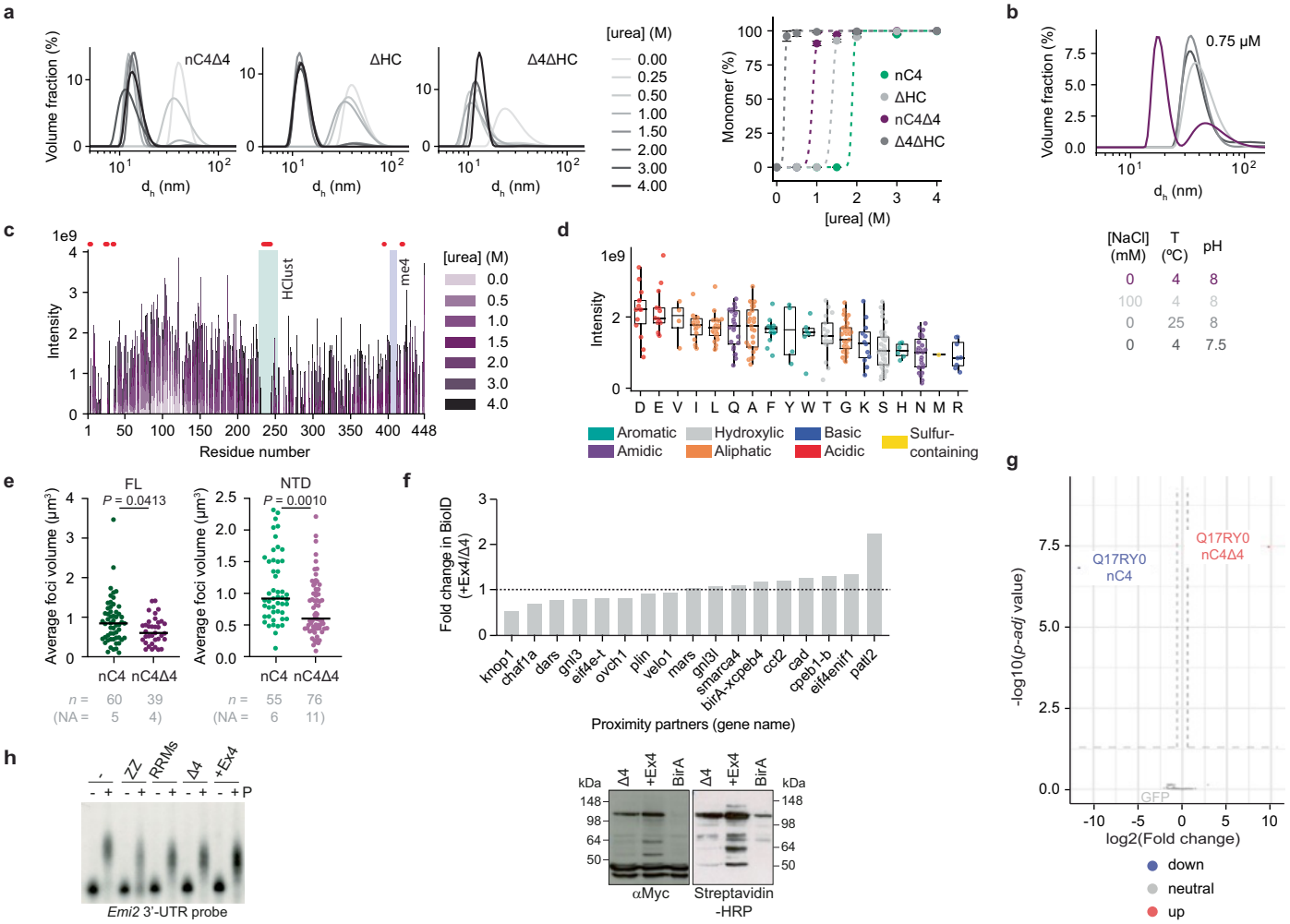

Extended Data Fig. 4 | Effect of me4 on nCPEB4(NTD) multimerization and on nCPEB4 interactions in cells. a) Left: urea titration monitored by DLS of nCPEB4Δ4(NTD), ΔHC, and Δ4ΔHC (100 μM protein, 5 °C). Right: relative volume fractions of the monomer and multimer peaks (mean ± s.d.) versus urea concentration for all protein variants. Related to Extended Data Fig. 3i. $n = 3$ measurements. **b)** Effect of concentration, temperature, ionic strength, and pH on nCPEB4Δ4(NTD) multimer formation monitored by DLS (representative of $n = 3$ measurements). **c)** $^{1}H,^{15}N$-CP-HISQC backbone amide peak intensities of nCPEB4Δ4(NTD) at increasing urea concentrations (100 μM protein, 5 °C). To simplify the comparison there is a gap in the amino acid sequence corresponding to me4 and the numbering of residues after this position is based on nCPEB4(NTD). Red dots: residues not assigned. $n = 1$ spectrum. **d)** Ranking of mean $^{1}H,^{15}N$-CP-HISQC backbone amide peak intensities of nCPEB4Δ4(NTD) at 4 M urea by amino acid type (100 μM protein, 5 °C). Box plots: line, median; box, quartiles; whiskers, 1.5x interquartile range. $n = 1$ spectrum. **e)** nCPEB4 and nCPEB4Δ4 number and size of foci from fluorescence microscopy of fixed N2a cells (median, two-tailed Mann-Whitney test). n, cells from 3 independent experiments. Related to Fig. 3c,d. **f)** xCPEB4 and xCPEB4 + Ex4 proximity partners determined by BioID in *Xenopus laevis* prophase I oocytes. Upper: fold increase in association of proximity partners with xCPEB4 harboring exon4 (+Ex4) relative to the xCPEB4 variant without exon4 (Δ4), shown as peptide-spectrum match (PSM) ratios between the two isoforms. Identified hits include proteins enriched in xCPEB4-BirA (Δ4) and xCPEB4 + Ex4-BirA, relative to BirA alone. The hits were identified in the N-terminal and C-terminal BirA fusions. Lower: WB of *X. laevis* oocytes injected with BirA alone or myc-tagged xCPEB4-BirA (Δ4) and xCPEB4 + Ex4-BirA (+Ex4) used in BioID assay. Biotinylated proteins shown with streptavidin-HRP. $n = 1$ independent biological replicate. **g)** Comparison of nCPEB4 and nCPEB4Δ4 interactomes composition in N2a cells determined by immunoprecipitation followed by mass spectrometry identification. Volcano plot showing differentially abundant interactome hits in nCPEB4Δ4 compared to nCPEB4. Bait proteins are indicated (nCPEB4Δ4: Q17RY0_nC4Δ4, nCPEB4: Q17RY0_nC4). Significance assessed with two-sided Empirical Bayes Statistics for Differential Expression test. **h)** Effect of me4 in nCPEB4 binding to RNA determined by in vivo competition assay. Polyadenylation of *Emi2* 3′-UTR radioactive probe in the absence (–) and presence (+) of progesterone (P) in *X. laevis* oocytes not injected (0% competition) or injected with CPEB1 RNA-binding domain (ZZ) (100% competition), CPEB4 RNA-binding domain (RRMs), xCPEB4 (Δ4), xCPEB4 + Ex4 (+Ex4). $n = 1$ independent experiment. nC4, nCPEB4; nC4Δ4, nCPEB4Δ4. For gel source data, see Supplementary Fig. 3.

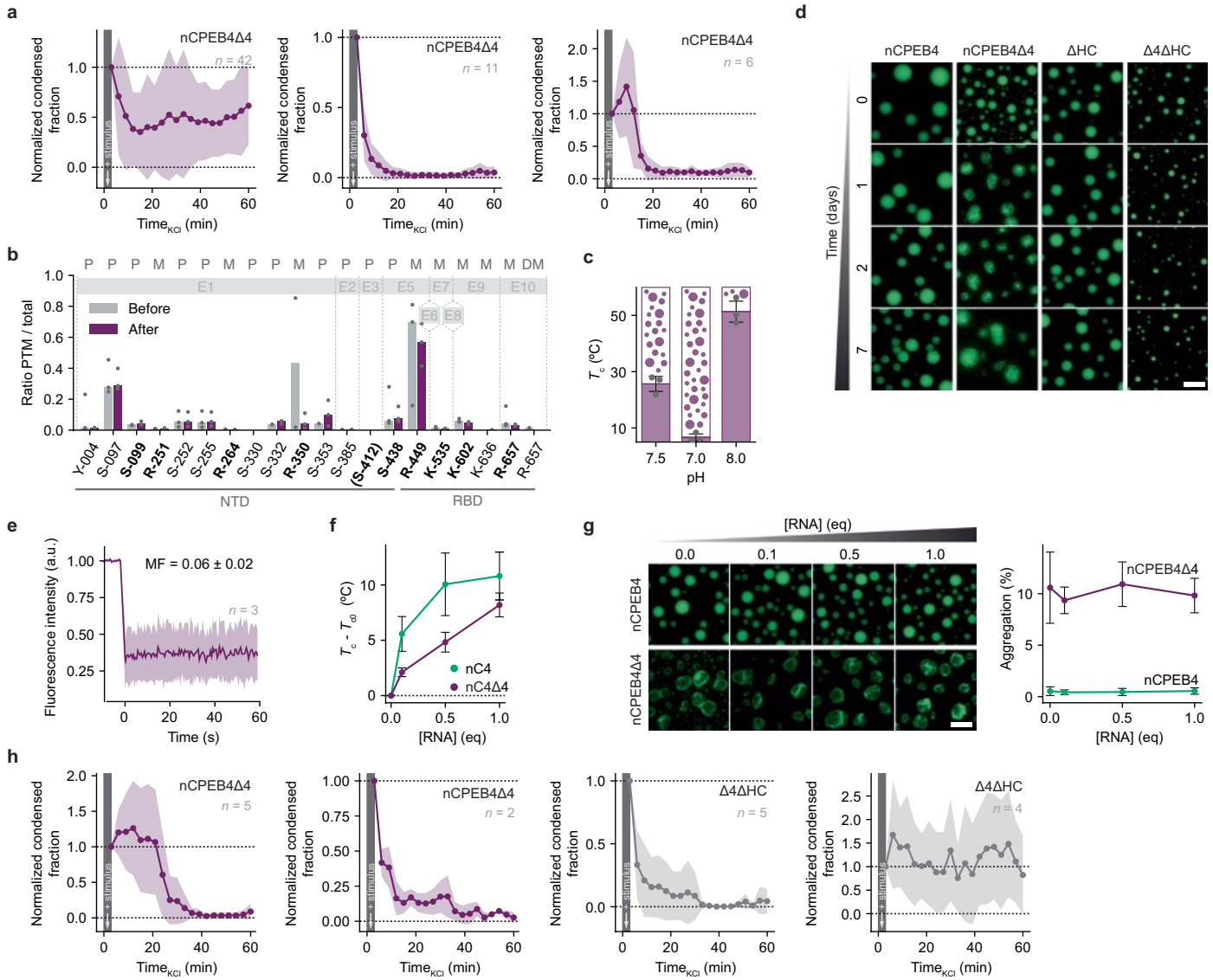

Extended Data Fig. 5 | Effect of me4 on condensate morphology in vitro and condensate dissolution in cells. a) Fraction of cellular area occupied by nCPEB4Δ4 condensates after stimulation, normalized to the value measured at the end of stimulation. Representation of the behavior of 71.2%, 18.6%, and 10.2% of cells (mean ± s.d.). *n*, cells out of 59 total cells. **b)** nCPEB4Δ4 modified-to-total occurrence ratios determined by mass spectrometry before and after stimulation of N2a cells overexpressing FL nCPEB4Δ4-GFP (median). *n* = 3 independent biological replicates. Bold: previously undescribed post-translationally modified sites. Gray line: positions of exons (E1-E10). P, phosphorylation; M, methylation; DM, dimethylation. **c)** Cloud point (mean ± s.d.) of nCPEB4Δ4(NTD) as a function of pH (10 µM protein, 100 mM NaCl). *n* = 3 independent measurements. **d)** Fluorescence microscopy of nCPEB4(NTD), nCPEB4Δ4(NTD), ΔHC, and Δ4ΔHC over time (30 µM protein, 200 mM NaCl, 37 °C). Related to Fig. 3h,i. *n* = 9 fields of view from 3 independent experiments. **e)** FRAP of in vitro nCPEB4Δ4(NTD) condensates (30 µM protein, 200 mM NaCl, 37 °C) after 7 days (mean ± s.d.). *n*, condensates. **f)** Change of the cloud point (mean ± s.d.) of nCPEB4(NTD) and nCPEB4Δ4(NTD) with increasing molar equivalents of RNA, relative to that measured without RNA (T_c-T_{c0}) (30 µM protein, 100 mM NaCl). nC4, nCPEB4; nC4Δ4, nCPEB4Δ4. *n* = 3 independent experiments. **g)** Fluorescence microscopy of nCPEB4(NTD) and nCPEB4Δ4(NTD) with increasing molar equivalents of RNA 1 day after sample preparation and aggregation quantification (mean ± s.d.) (30 µM protein, 200 mM NaCl, 37 °C). *n* = 9 fields of view from 3 independent experiments. **h)** Fraction of cellular area occupied by condensates after stimulation, normalized to the value measured at the end of stimulation, of live N2a cells overexpressing nCPEB4Δ4 and Δ4ΔHC mutant. Representation of the behavior of 22.7% and 9.1% (nCPEB4Δ4) and 26.3% and 21.1% (Δ4ΔHC) of cells (mean ± s.d.). *n*, cells out of 22 and 19 total cells, respectively. Related to Fig. 3m. For *a*,*h*, only cells showing cytoplasmic foci before stimulation were analyzed. Scale bars, 10 µm (*d*,*g*).

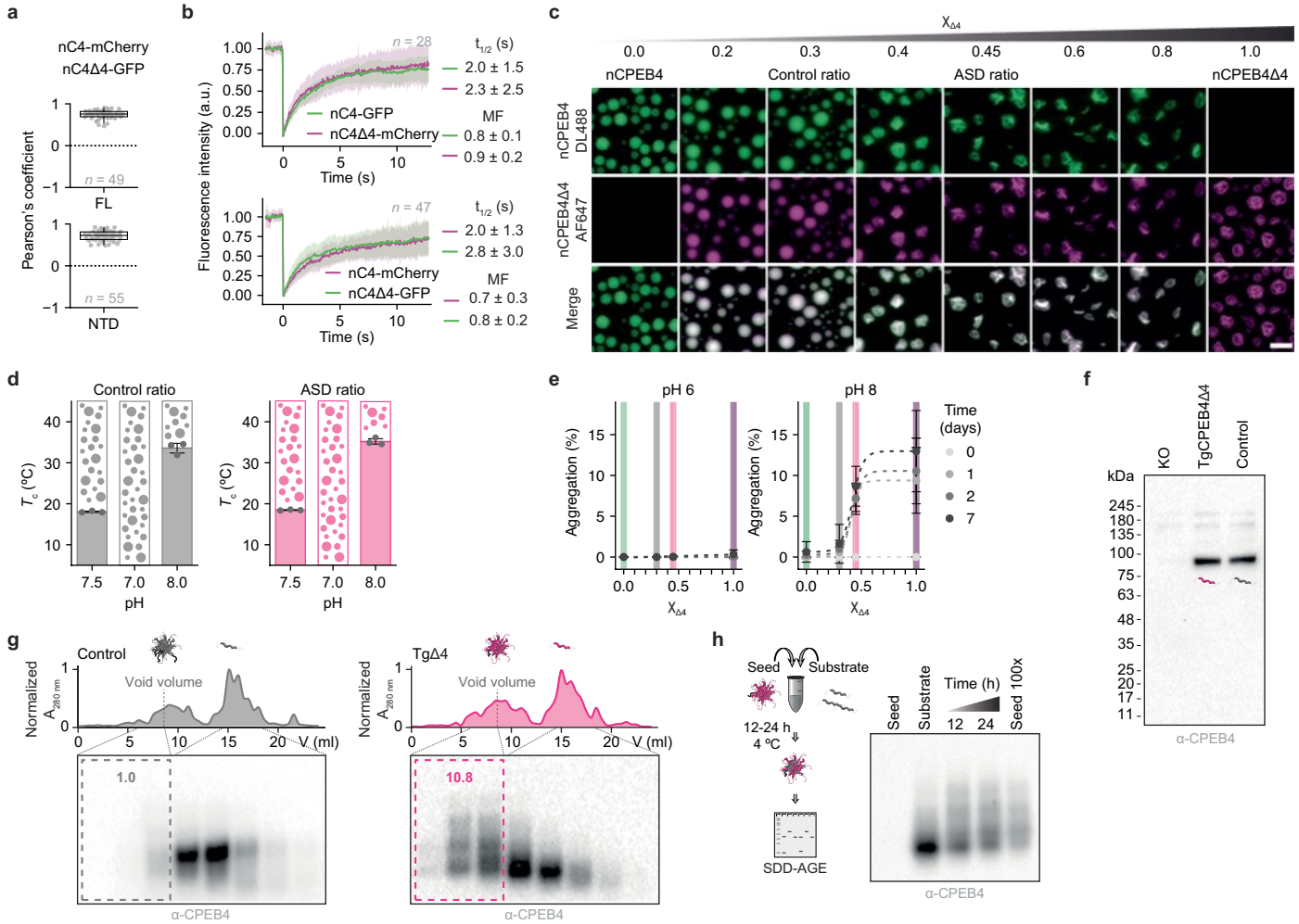

Extended Data Fig. 6 | Effect of nCPEB4Δ4 mole fraction on condensation in vitro and identification of nCPEB4 aggregates in mouse brains. **a)** Co-localization as assessed by using Pearson's correlation coefficient of fixed N2a cells co-transfected with nCPEB4-mCherry and nCPEB4Δ4-GFP. Box plots: line, median; box, quartiles; whiskers, 1.5x interquartile range. *n*, cells from 3 independent experiments. **b)** FRAP experiment (mean ± s.d.) in N2a cells co-transfected with FL nCPEB4-GFP and nCPEB4Δ4-mCherry (upper) or nCPEB4-mCherry and nCPEB4Δ4-GFP (lower). *n*, condensates from 3 independent experiments. **c)** Fluorescence microscopy of solutions of nCPEB4(NTD) and nCPEB4Δ4(NTD) of different compositions after 1 day (30 µM protein, 200 mM NaCl, 37 °C). *n* = 10 fields of view from 3 independent experiments. Related to Fig. 4d,e. Scale bar, 10 µm. **d)** Cloud point (mean ± s.d.) of control and ASD isoform ratio samples as a function of pH (10 µM protein, 100 mM NaCl). *n* = 3 independent measurements. **e)** Aggregation quantification (mean ± s.d.) of solutions of nCPEB4(NTD) and nCPEB4Δ4(NTD) of different compositions at pH 6 and 8 (30 µM protein, 200 mM NaCl, 37 °C). *n* = 9 fields of view from 3 independent experiments. **f)** WB of ex vivo CPEB4 from 6-month-old control mice, TgCPEB4Δ4 mice, and *Cpeb4* KO mice (negative control) brains by 4–12% gradient SDS-PAGE. *n* = 2 individual measurements. **g)** WB of different conformational states of ex vivo CPEB4 from 6-month-old control mice and TgCPEB4Δ4 mice brains using SDD-AGE. The increased amount of aggregated CPEB4 in TgCPEB4Δ4 mice brains, eluting in the void volume (framed fractions), was quantified and normalized to control mice, used as an internal control (10.8 vs 1.0). *n* = 2 individual measurements. **h)** Aggregation time course of monomeric CPEB4 from 6-month-old control mice brains seeded by stable CPEB4 aggregates from 6-month-old TgCPEB4Δ4 mice brains. The seed (~40 ng of total protein extracted) is undetectable in the WB. Within 24 h, CPEB4 monomers from 6-month-old control mice brains are aggregated, resembling the seed. The last lane displays the seed concentrated 100-fold. *n* = 2 individual measurements. nC4, nCPEB4; nC4Δ4, nCPEB4Δ4; TgΔ4, TgCPEB4Δ4. For gel source data, see Supplementary Fig. 4.

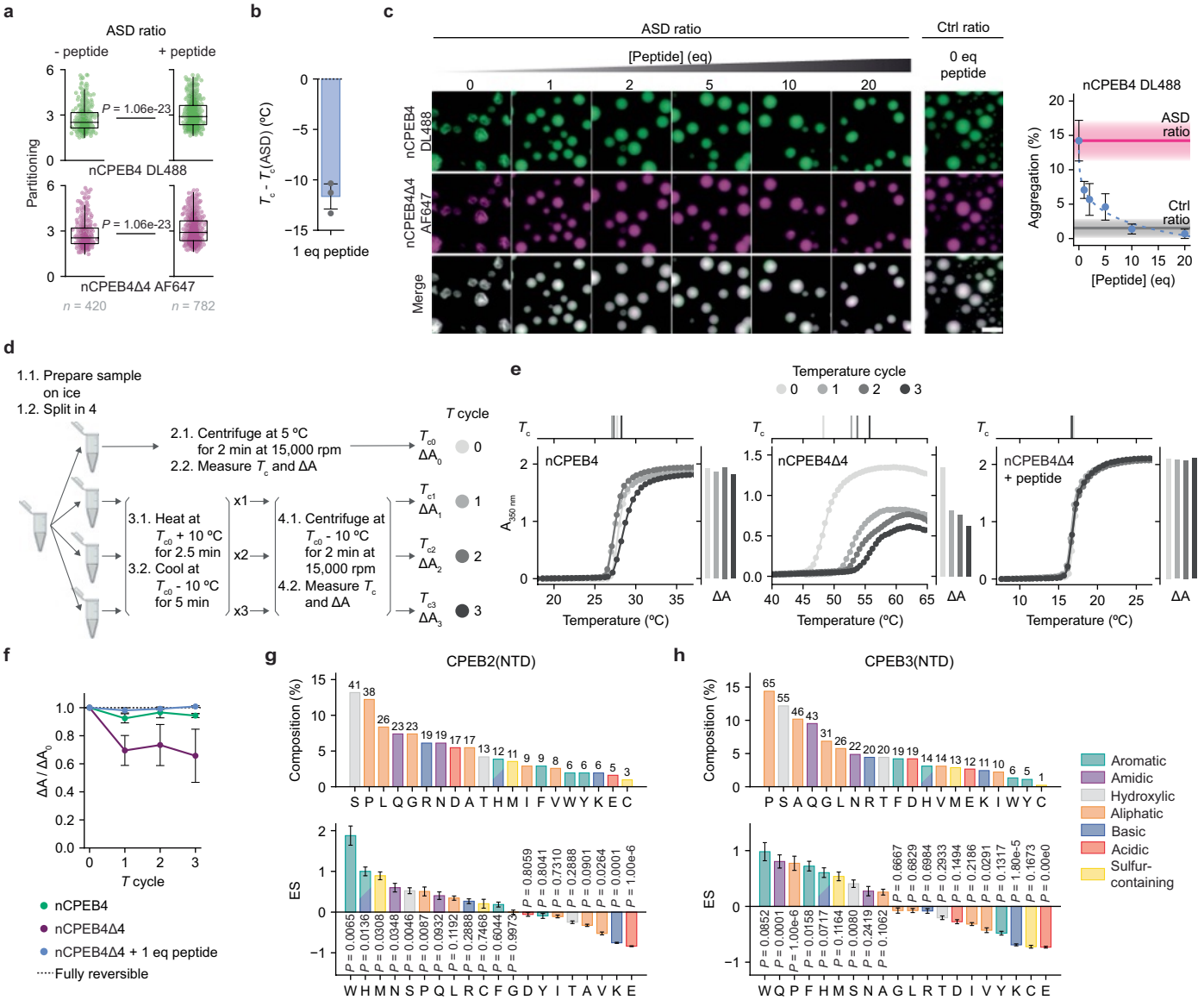

Extended Data Fig. 7 | Effect of the peptide on nCPEB4(NTD) condensation in vitro. a) Partitioning of each isoform in the condensates of an ASD ratio sample ($\chi_{\Delta 4}$ = 0.45) in the absence and presence of 1 molar equivalent of peptide (30 µM protein, 100 mM NaCl, 37 °C). Related to Fig. 5b. Box plots: line, median; box, quartiles; whiskers, 1.5x interquartile range. *n*, condensates. Statistical significance from a two-tailed Mann-Whitney test. **b)** Cloud point difference (mean ± s.d.) of an ASD ratio sample with 1 molar equivalent of peptide compared to the sample without peptide (T_c-T_c(ASD)) (30 µM protein, 100 mM NaCl). *n* = 3 independent measurements. **c)** Fluorescence microscopy of an ASD ratio sample (30 µM protein, 100 mM NaCl, 37 °C) with increasing molar equivalents of peptide after 1 day and aggregation quantification of nCPEB4 DL488 (mean ±s.d.). *n* = 9 fields of view from 3 independent experiments. Scale bar, 10 µm. **d)** Schematic representation of the temperature reversibility experiment. **e)** Example of one replicate of the temperature reversibility experiment. Apparent absorbance measurement for nCPEB4(NTD) (left), nCPEB4Δ4(NTD) (center), and nCPEB4Δ4(NTD) with 1 molar equivalent of peptide (right) over three temperature cycles. **f)** Temperature reversibility experiment monitored by apparent absorbance measurements (20 µM protein, 100 mM NaCl). Absorbance increase (ΔA) ratio (mean ± s.d.) at each temperature cycle relative to the ΔA measured before the first cycle ($\Delta A/\Delta A_0$). *n* = 3 independent measurements. Dotted line: fully reversible process. **g,h)** Amino acid composition and enrichment score (ES, mean ± s.d.) of each amino acid type in CPEB2(NTD) (*g*) and CPEB3(NTD) (*h*) compared to the DisProt3.4 database[84,85]. Illustration in *d* created using BioRender (credit: R.M., https://biorender.com/q89v018; 2023).

nature portfolio

Corresponding author(s): Raúl Méndez
Xavier Salvatella

Last updated by author(s): Oct 9, 2024

Reporting Summary

Nature Portfolio wishes to improve the reproducibility of the work that we publish. This form provides structure for consistency and transparency in reporting. For further information on Nature Portfolio policies, see our Editorial Policies and the Editorial Policy Checklist.

Statistics

For all statistical analyses, confirm that the following items are present in the figure legend, table legend, main text, or Methods section.

n/a	Confirmed
☐	☒ The exact sample size (*n*) for each experimental group/condition, given as a discrete number and unit of measurement
☐	☒ A statement on whether measurements were taken from distinct samples or whether the same sample was measured repeatedly
☐	☒ The statistical test(s) used AND whether they are one- or two-sided *Only common tests should be described solely by name; describe more complex techniques in the Methods section.*
☒	☐ A description of all covariates tested
☐	☒ A description of any assumptions or corrections, such as tests of normality and adjustment for multiple comparisons
☐	☒ A full description of the statistical parameters including central tendency (e.g. means) or other basic estimates (e.g. regression coefficient) AND variation (e.g. standard deviation) or associated estimates of uncertainty (e.g. confidence intervals)
☐	☒ For null hypothesis testing, the test statistic (e.g. *F*, *t*, *r*) with confidence intervals, effect sizes, degrees of freedom and *P* value noted *Give P values as exact values whenever suitable.*
☒	☐ For Bayesian analysis, information on the choice of priors and Markov chain Monte Carlo settings
☒	☐ For hierarchical and complex designs, identification of the appropriate level for tests and full reporting of outcomes
☐	☒ Estimates of effect sizes (e.g. Cohen's *d*, Pearson's *r*), indicating how they were calculated

Our web collection on statistics for biologists contains articles on many of the points above.

Software and code

Policy information about availability of computer code

Data collection	Molecular simulations were performed using openMM v7.5 (https://openmm.org/).
Data analysis	Simulations were analysed using OVITO Basic (v.3.7), MDTraj (v.1.9.6), and MDAnalysis (v.1.1). Molecular visualisations were generated using VMD (v.1.9.4). Custom code used to generate and analyse data is available at https://github.com/KULL-Centre/_2023_Garcia-Cabau_CPEB4 and at Zenodo (https://doi.org/10.5281/zenodo.13880099). NMR backbone resonance assignments were performed using CcpNmr 2.4.2. Experiments were processed using qMDD 3.2, NMRPipe and Topspin 4.0.8 (Bruker). Diffusion coefficients were obtained using MestreNova v14.2.1-27684.

For manuscripts utilizing custom algorithms or software that are central to the research but not yet described in published literature, software must be made available to editors and reviewers. We strongly encourage code deposition in a community repository (e.g. GitHub). See the Nature Portfolio guidelines for submitting code & software for further information.

Data

Policy information about availability of data

All manuscripts must include a data availability statement. This statement should provide the following information, where applicable:

- Accession codes, unique identifiers, or web links for publicly available datasets
- A description of any restrictions on data availability
- For clinical datasets or third party data, please ensure that the statement adheres to our policy

The NMR assignments are available on BMRB (ID 51875 and 52346). The simulation data generated in this study are available via https://github.com/KULL-Centre/_2023_Garcia-Cabau_CPEB4. Protein sequences correspond to UniProt IDs Q17RY0 for CPEB4, Q7Z5Q1 for CPEB2, and Q7TN99 for CPEB3. The rest of the data are included in this article as source data.

Human research participants

Policy information about studies involving human research participants and Sex and Gender in Research.

Reporting on sex and gender	N/A
Population characteristics	N/A
Recruitment	N/A
Ethics oversight	N/A

Note that full information on the approval of the study protocol must also be provided in the manuscript.

Field-specific reporting

Please select the one below that is the best fit for your research. If you are not sure, read the appropriate sections before making your selection.

☒ Life sciences ☐ Behavioural & social sciences ☐ Ecological, evolutionary & environmental sciences

For a reference copy of the document with all sections, see nature.com/documents/nr-reporting-summary-flat.pdf

Life sciences study design

All studies must disclose on these points even when the disclosure is negative.

Sample size	Sample size was empirically established in accordance with previous experience with similar experiments and based on the variability of previous similar data. the distribution and reproducibility of the data were also taken into account to choose sample size for each experiment. No statistical test was performed to predetermine sample size. Accordingly, we performed n=3 for the majority of experiments.
Data exclusions	No data were excluded from the analyses.
Replication	Images of primary striatal neurons in Fig. 1c and Extended Fig. 1d are representative of two independent experiments. Live-cell time-lapse movies of striatal neurons in Fig. 1d and Extended Fig. 1e were acquired once and images show representative behavior from all imaged cells. Live-cell acquisition of NTD nCPEB4-GFP in Fig. 1h and Extended Fig. 1i was performed twice. RT-PCRs monitoring CPEB4 splicing in Ext. Fig. 1b and Srrm4 in qRT-PCRs in Ext. Fig 1c were performed twice. qRT-PCRs monitoring nCPEB4 isoforms and splicing factors in cell lines were performed in n >= 1. Ionomycin experiments in Ext. Fig 1c were replicated twice. BioID and RNA competition experiments in Ext. Fig 4b,c were performed once. Live-cell acquisition of NTD nCPEB4-GFP 12A in Fig. 2b and Extended Fig. 2b was performed once and images show representative behavior from all imaged cells. All the other results were replicated at least in three independent biological replicates, as indicated in the manuscript.
Randomization	For the comparison of the fate of the condensates formed by nCPEB4 variants upon depolarization (Fig. 1j, Fig. 3f, Fig. 3l and Extended Data Fig. 2e), all samples were randomly allocated into experimental groups. Moreover, time-lapses from different variants (different experimental groups) were acquired in a different order for different biological replicates to avoid biases due to the time of incubation post-transfection. For all other experiments, all samples were randomly allocated into experimental groups when possible. Moreover, in all other experiments, different experimental groups were simultaneously and equally analyzed.
Blinding	The investigators were blinded to group allocation during data analysis in all experiments involving qualitative analysis of the data of more than one group of data. These experiments include quantification of the percentage of cells displaying cytoplasmic foci after depolarization (Fig. 1j, Fig. 3f, Fig. 3l and Extended Data Fig. 2e) was performed blindly. For the rest of the experiments, quantitative analysis of the data was performed without the need of blinding since specific quantifications were equally applied to all the groups analyzed by the specified used

softwares.

Reporting for specific materials, systems and methods

We require information from authors about some types of materials, experimental systems and methods used in many studies. Here, indicate whether each material, system or method listed is relevant to your study. If you are not sure if a list item applies to your research, read the appropriate section before selecting a response.

Materials & experimental systems

n/a	Involved in the study
☐	☒ Antibodies
☐	☒ Eukaryotic cell lines
☒	☐ Palaeontology and archaeology
☐	☒ Animals and other organisms
☒	☐ Clinical data
☒	☐ Dual use research of concern

Methods

n/a	Involved in the study
☒	☐ ChIP-seq
☒	☐ Flow cytometry
☒	☐ MRI-based neuroimaging

Antibodies

Antibodies used

For WB, we used the following antibodies:
- Primary antibodies: anti-CPEB4 (homemade, mouse monoclonal, clone 149C), anti-GFP (Invitrogen, rabbit polyclonal, A6455), anti-myc (Abcam, goat polyclonal, ab9132), HRP anti-β actin (Abcam, mouse monoclonal, ab20272); or streptavidin (Thermofisher, S911).
- Secondary antibodies: goat anti-mouse (Thermofisher, 31430), goat anti-rabbit (Thermofisher, G-21234), donkey anti-goat (Abcam, ab6885).

For IHC, we used rabbit polyclonal anti-CPEB4 antibody (Abcam, ab83009).
For IF, we used the following antibodies:
- Primary antibody: anti-CPEB4 antibody (clone 149C).
- Secondary antibody: Alexa 488 Donkey anti-mouse (Thermofisher, A-21202).

Validation

All commercial antibodies were validated by the provider and extensively used in previous studies. Home-made anti-CPEB4 antibody was validated by CPEB4 knock-down or knock-out in multiple eukaryotic cell lines and mice models.

Antibodies used for WB:
- Primary antibodies: anti-CPEB4 antibody (homemade, mouse monoclonal, clone 149C) as detailed above, was validated by CPEB4 knock-down or knock-out in multiple eukaryotic cell lines and mice models; anti-GFP antibody (Invitrogen, rabbit polyclonal, A6455) was validated by the provider in western blot by detection of different proteins fused with GFP that were transiently transfected in human cells; anti-myc antibody (Abcam, goat polyclonal, ab9132) reactivity was validated by the provider in WB with myc tag samples and was used in previous studies including Duran-Arqué et al., Genome Biology, 2022; HRP-anti-β actin (Abcam, mouse monoclonal, ab20272) was validated by the provider for WB in mouse, human and rat and was used in previous studies including Yu et al., Cell, 2021; streptavidin (Thermofisher, S911) was validated for WB in previous studies including Branon et al., 2018, Nat Biotechnol. by addition of exogenous biotin to human cell lines for similar purposes to the ones in this study (e.g. TurboID).

Antibodies used for IHC:
Rabbit polyclonal anti-CPEB4 antibody (Abcam, ab83009) was validated by CPEB4 knock-down or knock-out in multiple eukaryotic cell lines and mice models.

Antibody used for IF: anti-CPEB4 antibody (homemade, mouse monoclonal, clone 149C) was validated as indicated in the WB section.

Eukaryotic cell lines

Policy information about cell lines and Sex and Gender in Research

Cell line source(s)

Neuro-2a (N2a) cell line was purchased from ATCC (CCL-131).
NmumG cell line was a gift from Antonio García de Herreros.
C2C12 cell line was a gift from Antonio Zorzano.

Authentication

None of the cells used were further authenticated, since they are commercial cell lines and were used at low passages.

Mycoplasma contamination

Mycoplasma contamination was checked bi-monthly and all cell lines always tested negative.

Commonly misidentified lines
(See ICLAC register)

No commonly misidentified cell lines in accordance with the ICLAC database were used in this study.

Animals and other research organisms

Policy information about studies involving animals; ARRIVE guidelines recommended for reporting animal research, and Sex and Gender in Research

Laboratory animals	For striatal neurons extraction, C57BL/6J mice over 6 weeks of age were crossed in timed matings. For RNA extraction from tissues, B6.129 mice over 6 weeks of age were used. For CPEB4 IHC in mice, C57BL/6J mice embryos at embryonic day 13.5 were used. For BioID and competition experiments, adult Xenopus laevis (over 36 months of age) were used. For the in vivo conformation of CPEB4 studies we used - Homozygous CPEB4 KO mice in C57BL/6J background. - TgCPEB4Δ4 mice in C57BL/6J background. Animals of 1.5 and 6 months were used. All mice were bred and housed in the CBMSO animal facility. Mice were grouped four per cage with food and water available ad libitum and maintained in a temperature-controlled environment on a 12 h–12 h light–dark cycle with light onset at 08:00 and a relative humidity of 55 ± 10%. Animal housing and maintenance protocols followed local authority guidelines.
Wild animals	The study did not involve wild animals.
Reporting on sex	For striatal neurons extraction, mice females with an increment over 3 grams up to 18 days after a positive plug were euthanized and embryos were collected at E18.5. Striatal neurons from all mice embryos were extracted regardless of their sex. For BioID and competition experiments, stage VI oocytes were obtained from adult Xenopus laevis females as previously described in [de Moor and Richter, EMBO, 1999]. For the in vivo conformation of CPEB4 studies both male and female mice were included in similar proportions.
Field-collected samples	This study did not involve samples collected from the field.
Ethics oversight	All experiments with mouse models and Xenopus laevis were approved by the the Animal Ethics Committee at the Barcelona Science Park (PCB) and by the Government of Catalonia. For the in vivo conformation of CPEB4 studies Animal experiments were performed under protocols approved by the CBMSO Animal Care and Utilization Committee (Comité de Ética de Experimentación Animal del CBMSO, CEEA-CBMSO), and Comunidad de Madrid (PROEX 247.1/20). In accordance with the current regulation, all requirements for the investigation were assessed by the Animal Testing Commission as the organization authorized by the Government of Catalonia, including the information related to the use of anesthesia during the project, the origin of the animals, information related to housing, zootechnical and care conditions of the animals in the project, the information related to the euthanasia method, the information presented in relation to the accreditation/training of the personnel participating in the project, the compliance with the 3Rs and the damages and benefits of the project were assessed in the frame of ethical balance.

Note that full information on the approval of the study protocol must also be provided in the manuscript.